Simulation of Inviscid Compressible Flows Using PDE Transform

Langhua Hu[1], Siyang Yang[1] and Guo-Wei Wei[1,2,3,∗]

[1] *Department of Mathematics, Michigan State University, MI 48824, USA.*
[2] *Department of Electrical and Computer Engineering, Michigan State University, MI 48824, USA.*
[3] *Center for Mathematical Molecular Biosciences, Michigan State University, MI 48824, USA.*

Abstract. The solution of systems of hyperbolic conservation laws remains an interesting and challenging task due to the diversity of physical origins and complexity of the physical situations. The present work introduces the use of the partial differential equation (PDE) transform, paired with the Fourier pseudospectral method (FPM), as a new approach for hyperbolic conservation law problems. The PDE transform, based on the scheme of adaptive high order evolution PDEs, has recently been applied to decompose signals, images, surfaces and data to various target functional mode functions such as trend, edge, texture, feature, trait, noise, etc. Like wavelet transform, the PDE transform has controllable time-frequency localization and perfect reconstruction. A fast PDE transform implemented by the fast Fourier Transform (FFT) is introduced to avoid stability constraint of integrating high order PDEs. The parameters of the PDE transform are adaptively computed to optimize the weighted total variation during the time integration of conservation law equations. A variety of standard benchmark problems of hyperbolic conservation laws is employed to systematically validate the performance of the present PDE transform based FPM. The impact of two PDE transform parameters, i.e., the highest order and the propagation time, is carefully studied to deliver the best effect of suppressing Gibbs' oscillations. The PDE orders of 2-6 are used for hyperbolic conservation laws of low oscillatory solutions, while the PDE orders of 8-12 are often required for problems involving highly oscillatory solutions, such as shock-entropy wave interactions. The present results are compared with those in the literature. It is found that the present approach not only works well for problems that favor low order shock capturing schemes, but also exhibits superb behavior for problems that require the use of high order shock capturing methods.

∗Corresponding author. *Email addresses:* `hulanghu.at.msu.edu@gmail.com` (L. Hu), `yangsiyang@gmail.com` (S. Yang), `wei@math.msu.edu` (G.-W. Wei)

1 Introduction

Hyperbolic systems of nonlinear conservation laws

$$\mathbf{u}_t + \mathbf{f}(\mathbf{u})_x = 0 \tag{1.1}$$

with an initial condition

$$\mathbf{u}(x,0) = \mathbf{u}_0(x) \tag{1.2}$$

have attracted great attention in the past few decades in mathematical, scientific and engineering communities due to their practical applications in fluid mechanics, aerodynamics, and nano-bio systems, to mention only a few. The solution to this class of problems may not exist in the classical sense because of possible discontinuities in the initial condition, material interface, singularity formation, turbulence, blow-up, etc.

Both global and local methods have been developed for hyperbolic conservation laws. Many up-to-date local methods have been proposed for shock-capturing, turbulence and shock interaction, including weighted essentially non-oscillatory (WENO) scheme [21, 23, 37, 38], central schemes [3, 27, 31, 34], arbitrary-order non-oscillatory advection scheme [43], gas kinetic [30, 35, 58], anisotropic diffusion [36], conjugate filters [19] and image processing based algorithms [17, 52]. An important factor that contributes to the success of the above mentioned local schemes in the shock-capturing is their appropriate amount of intrinsic numerical dissipation, which is introduced either by explicit artificial viscosity, upwinding, relaxation, or by local average strategy in non-oscillatory central schemes [24]. Indeed, the characteristic decomposition based on Roe's mean matrix can also be considered as a local average of the Jacobian matrix. The relation between some approximate Riemann solvers and relaxation schemes was analyzed by LeVeque [29]. Local characteristic decomposition is not necessary in low-order methods because of intrinsic numerical dissipation, while it seems to be indispensable in high-order methods [38]. In general, local and low order methods perform well for problems whose Fourier responses of the solution focus predominantly in the low frequency region. For this class of problems, first order or second order Godunov type of schemes can be very efficient in balancing accuracy and efficiency. When local and low order methods are used for resolving shocks in flows with fine structural details or highly oscillatory patterns, their numerical dissipation is usually too large to offer informative results.

Spectral methods, or global methods, on the contrary, produce little numerical dissipation and dispersion in principle when applied to approximate spatial derivatives. It is well known that spectral methods are some of the most accurate and efficient approaches for solving partial differential equations (PDEs) arising from scientific and engineering

applications [5, 12, 44]. Therefore, it is highly desirable to use spectral methods for the solution of hyperbolic conservation laws, because the multiscale features, including Kolmogorov microscales, in the hyperbolic conservation law systems require high resolution methods. Nevertheless, when spectral methods are applied to the approximation of spatial derivatives of a discontinuous function, which often occurs in hyperbolic conservation law problems, one encounters Gibbs' oscillations [15]. Most previous investigations are aimed at improving the rate of convergence away from the discontinuity while recovering smooth solutions from the contamination of Gibbs' oscillations. The suppression of Gibbs' oscillations is necessary in order to avoid unphysical blow-ups in the time integration. Therefore, it has been of tremendous interest in modifying spectral methods for hyperbolic conservation law systems in the past two decades [28, 40]. There are two general types of approaches in spectral based methods for hyperbolic conservation law systems: (1) explicit artificial viscosity, e.g. spectral viscosity method proposed by Tadmor [42], and (2) filtering. It is expected that the appropriate use of spectral methods enables us not merely to capture the shock, but also to resolve the delicate features, immersed interface, and underlying fine structures of the flow.

Filters are designed to apply either in the spectral domain, called spectral filters, or in the physical domain. Typical spectral filters include Lanzos filter, raised cosine filter, sharpened raised cosine filter, Krasny filter [26] and exponential cutoff filter, as listed by Hussaini *et al.* [22]. More sophisticated and effective filters in spectral domain are Vandeven's pth order filter [45], and Gottlieb and Tadmor's regularized Dirichlet function [16]. A filter-based Reynolds-averaged Navier-Stokes approach was developed to improve the predictive capability considerably in comparison to the standard $k-\epsilon$ model [25].

Filters in the physical domain are also commonly used alternatives to spectral filters. In the framework of spectral methods, it is generally more difficult to design appropriate filters in the physical domain than in the Fourier domain. A simple procedure is to make use of numerical dissipation contained in some *high-order* shock-capturing schemes [4], such as the ENO scheme, where, actually, numerical dissipation was introduced both in the Fourier domain (via an exponential filter) and in the physical domain (via ENO polynomial filter). Such a strategy was employed by Yee *et al.* [59] to construct characteristic filters in the framework of finite difference methods. Gegenbauer polynomials are used to resolve the oscillatory partial Fourier summation [15]. Promising numerical results were generated by using filter approaches [10, 11, 13].

About a decade ago, we proposed a conjugate filter oscillation reduction (CFOR) scheme [18, 40, 54, 61, 62] for hyperbolic conservation laws. This scheme was constructed within the framework of a local spectral wavelet method, namely, the discrete singular convolution (DSC) algorithm [46, 50, 56]. Here, 'conjugate filters' means that the effective wavenumber range of the low-pass filter is largely overlapped with that of the high-pass filter used for the approximation of spatial derivatives. In fact, the DSC algorithm is used to behave as both low-pass filters and high-pass filters. Extensive validation of the CFOR scheme over a wide range of shock-capturing problems has been carried out [18, 54, 61, 62]. We demonstrated that CFOR scheme provides some of the highest

grid resolution, i.e., 5 points per wavelength (PPW), for the interaction of shock and entropy waves, and for many other challenging problems involving natural high frequency oscillations [40, 61, 62].

Despite great effort in the past few decades, the efficient application of filters for hyperbolic conservation law systems remains a challenging problem. To design efficient filter methods, one must control a number of filter properties, such as flatness, ripple, filter length, effective frequency range and length of transition band, to name only a few. Normally, it is desirable to utilize filters that are free of dispersion errors, flat while having very small transition band, short in length while having high resolution. Obviously, some of these properties are conflicting with each other. Adjustable parameters have to be employed to tune filter properties in the application. In addition to the difficulties in controlling filter properties, there are intrinsic mathematical challenges in developing filtered spectral methods. First, the solutions to different hyperbolic conservation law equations may have different Fourier spectral distributions. Additionally, even for a single conservation law equation, the characteristic of the Fourier spectral distribution may change during the time integration. Finally, the same conservation law equation can exhibit dramatically different Fourier spectral distributions when it is applied to different physical problems, i.e., problems with different initial, interface and boundary conditions. Therefore, an optimal filter has to be fully adaptive to hyperbolic equations, to initial, interface and boundary conditions, and to the variation of spectral characteristic during the time integration. Unfortunately, such a filter approach still does not exit yet. Given the complexity in the hyperbolic conservation law and in filter properties, it is unlikely that there will be a perfect solution to these challenges in the near future. Consequently, these challenging and important problems call for the further study of spectral filter approaches.

Most recently, we have introduced PDE transform as a new approach for the analysis of signals, images, surfaces and data [47, 49, 60]. The PDE transform is a PDE based systematical approach for decomposing signals, images, and data into functional modes, which exhibit appropriate time-frequency localizations. Like wavelet transform, the PDE transform is able to provide a perfect reconstruction. Unlike wavelet transform or Fourier transform, the PDE transform offers results in the physical domain. The PDE transform was constructed based on a family of arbitrarily high order nonlinear PDEs first introduced by Wei for edge-preserving image restoration in 1999 [51] and PDE based high-pass filters proposed by Wei and Jia in 2002 [55]. Variational models of PDE transform have also been proposed [47]. With a recursive procedure [48,49] to incorporate appropriate residues, i.e., initial conditions, the PDE transform is able to extract functional mode functions (FMFs). By FMFs, we mean the mode components which share same band of frequency distribution as well as same category of physical functions, i.e., trend, edge, texture, feature, trait, noise etc. Using the FMFs obtained from the PDE transform, secondary processing, or post-processing, can be performed to achieve desirable tasks, such as edge detection, trend estimation, image enhancement, denoising, texture quantification, segmentation, feature extraction, pattern recognition, etc. The PDE transform can

perform as tunable filters. By adjusting the order of the PDE transform, i.e., the highest order of the PDE, one controls time-frequency localization, while by adjusting the diffusion coefficients or propagation time, one obtains desirable frequency precision or multiresolution analysis [60]. The PDE transform can be tuned according to the input data to provide desirable mode information. The full process of the PDE transform is nonlinear even if linear PDEs are employed. Unlike the Fourier transform or the wavelet transform, the PDE transform conserves the data representation. The resulting functional modes are still in the original data form. The PDE transform has been applied to image analysis [47, 49], signal processing [48] and biomolecular surface construction [60]. High order PDE transforms with their order being much higher than 4 are found to play a vital role in signal analysis, image processing and surface generation.

The objective of present work is to explore the utility of the PDE transform for the solution of hyperbolic conservation laws. To avoid the strict stability constraints in solving high order PDEs and gain the desirable acceleration in the time integration, we make use of a fast PDE transform, i.e., the PDE transform realized by the fast Fourier transform in a single time stepping. Such a fast algorithm is paired with the Fourier pseudospectral method (FPM) for solving hyperbolic conservation law equations and suppressing Gibbs' oscillations. Since the PDE transform is implemented via the fast Fourier transform, it matches very well with the FPM. In fact, the PDE transform has an adjustable effective wavenumber range that makes it viable to capture fine flow structures, which is a desirable objective of spectral methods for hyperbolic conservation law systems. It is this adjustable effective wavenumber range that controls the resolution of the overall scheme. In our design, this adjustable effective wavenumber range can be varied by the highest order of the PDE transform and the duration of time propagation according to the resolution requirement of a hyperbolic conservation equation and the physical problem of interest. Different orders of the PDE transform have different magnitude responses and adjustability in the Fourier domain, which in turn influences the accuracy and resolution of the PDE transform based FPM. It is this flexibility that makes the present method applicable to a wide variety of hyperbolic conservation law systems. The performance of the proposed method is extensively validated and compared with those of other approaches in the literature.

The rest of this paper is organized as follows. Section 2 is devoted to a brief introduction of the theory and formulation of the PDE transform, which is useful for the understanding of the working principle of the present approach for shock capturing. The implementation of the PDE transform in the FPM will be presented. The proposed PDE transform based FPM is extensively validated in Section 3. We consider a variety of numerical experiments, including the linear advection equation, Burgers' equation, shock-tube problems, shock-entropy wave interaction, and shock-vortex interaction. The shock-capturing ability and the high resolution character of the present method are illustrated via these applications. The performance of the present method is compared with those of earlier schemes in the literature. A brief discussion of the proposed method is given in Section 4.

2 Theory and algorithm

To establish notation and enhance the basic understanding of the proposed PDE transform strategy for systems of hyperbolic conservation laws, we present a brief introduction of arbitrarily high order nonlinear PDEs and PDE transforms. The detailed numerical algorithm for time integration of evolution equations of hyperbolic conservation laws is described.

2.1 Arbitrarily high order PDEs

The PDE transform of arbitrarily high integer order PDEs has been introduced in our earlier work [47, 49]. Since variational approaches have found their success in a variety of scientific and engineering fields [2, 6–9, 39, 53, 57], a variational derivation of the PDE transform has also been presented [47, 60]. Here we briefly review the variational derivation of the PDE transform. Let $\mathbf{r} = (x, y, z) \in \mathbb{R}^3$ and denote by $\nabla = \partial / \partial \mathbf{r}$ a gradient operator in $\mathbb{R}^3$. For any integer $q > 0$, we consider the energy functional

$$E(u, \nabla^q u) = \int \left[\Lambda \left(|\nabla^q u|^2 \right) + \epsilon (X - u)^2 \right] d\mathbf{r}, \tag{2.1}$$

where ϵ is a constant, $\epsilon (X - u)^2$ is the fidelity term, X is the original data, and $\Lambda(\cdot)$ is an appropriate penalty function. Some of the most commonly used penalty functions include the Tikhonov form, the mean curvature form, and the Gaussian form [9, 32]. Minimizing the energy functional (2.1) by using the Euler-Lagrange equation, we have

$$\nabla^q \odot^q \Lambda_{uq} \left(|\nabla^q u|^2 \right) \nabla^q u + \epsilon (X - u) = 0, \tag{2.2}$$

where $\odot^q$ represents an appropriate inner product and

$$\Lambda_{uq} = (-1)^{q+1} \partial \Lambda / \partial |\nabla^q u|^2. \tag{2.3}$$

To efficiently solve Eq. (2.2), we introduce an artificial time t and convert it into a time-dependent PDE

$$\frac{\partial u}{\partial t} = \nabla^q \odot^q \Lambda_{uq} \left(|\nabla^q u|^2 \right) \nabla^q u + \epsilon (X - u). \tag{2.4}$$

Eq. (2.4) is essentially equivalent to our earlier variational derivation of the PDE transform [47], however, in our Ref. [47], there is a typo; specifically, in page 2003, $\Lambda_{uj}(\cdot)$ and $\Lambda_{vj}(\cdot)$ should be defined as $\Lambda_{uj}(\cdot) = (-1)^{j+1} \frac{\partial \Lambda_u}{\partial |D^j u|^2}$ and $\Lambda_{vj}(\cdot) = (-1)^{j+1} \frac{\partial \Lambda_v}{\partial |D^j v|^2}$, respectively.

2.2 PDE transform

One of the important properties of the PDE transform is its ability to iteratively extract mode functions from a given data $X(\mathbf{r})$. To illustrate this point, we denote the solution of Eq. (2.4) as $\check{X}(\mathbf{r},\tau)$ such that

$$\check{X}^k(\mathbf{r},\tau) = \mathcal{L}X^k(\mathbf{r},0), \tag{2.5}$$

where $\mathcal{L}$ is a low-pass PDE transform satisfying $\mathcal{L}u(\mathbf{r},0) = u(\mathbf{r},\tau)$, $\check{X}^k(\mathbf{r},\tau)$ are mode functions.

Here $X^k(\mathbf{r},0)$ is the kth residue function defined by

$$X^1(\mathbf{r},0) = X(\mathbf{r}) \tag{2.6}$$

and

$$X^k(\mathbf{r},0) = X^1(\mathbf{r},0) - \sum_{j=1}^{k-1} \check{X}^j(\mathbf{r},\tau), \quad \forall k = 2,3,\cdots. \tag{2.7}$$

Note that Eq. (2.7) defines the initial value for Eq. (2.5). Therefore, PDE transform is a set of iterations using arbitrarily high order PDEs discussed in the last section.

Obviously, like the wavelet transform, there is a perfect reconstruction of the original data $X(\mathbf{r})$ in terms of all the mode functions and the last residue

$$X(\mathbf{r}) = \sum_{j=1}^{k-1} \check{X}^j(\mathbf{r},\tau) + X^k(\mathbf{r},0). \tag{2.8}$$

Note that the PDE transform given in Eq. (2.5) *recursively* extracts mode functions based on the input residue function. This procedure is nonlinear even if a linear PDE operator is used because the initial value changes during the repeated operations.

The first mode produced by the PDE transform described above is the trend of the data. The residue of the trend is an edge function, including possible noisy components. By systematically repeating the low-pass PDE transform (2.5), one can extract all the desirable higher order mode functions. In our earlier work, high-pass PDE transforms were also constructed in which the first mode is edge type of information or possible noise; while the final residue is the trend [48].

The appropriate number of iterations needed for a given problem depends on the nature of the problem. To extract higher order mode functions, multiple iterations are required. However, for low-pass filtering, we just need one iteration of the PDE transform.

Solving arbitrarily high order PDEs, such as Eq. (2.4) in the PDE transform can be a very difficult issue for some practical application. A main difficulty is the stability constraint as the time stepping is normally proportional to the $2m$th power of spatial grid spacing, where $2m$ is the highest order of the PDE transform. An exception is digital image processing, in which the spatial grid spacing is usually unit and thus bypasses the

stability constraint. However, spatial grid spacing is normally smaller than one in most other applications.

There is another way that one can bypass the stability constraint entirely and obtain the solution in a single time step. This approach relies on the use of the fast Fourier transform (FFT) for the solution of evolution PDEs [40]. To this end, we linearize (2.4). Let us assume that a linear PDE has the form

$$\partial_\tau v = \sum_{j=1}^{m} (-1)^{j+1} d_j \nabla^{2j} v + \epsilon (X^k - v), \quad \tau \geq 0, \tag{2.9}$$

where $d_j > 0$, $\epsilon \sim 0$ and $X^k \in \mathbb{R}^n$ is the kth residue of the data. When Eq. (2.9) is subject to initial value $v(\mathbf{r}, 0) = X^k$ and periodic boundary conditions, it is exactly solvable in the n dimensional Fourier representation

$$\hat{\check{X}}^k = \hat{\mathcal{L}} \hat{X}^k, \tag{2.10}$$

where $\hat{\check{X}}$ and $\hat{X}^k$ are the Fourier transforms of $\check{X}^k$ and X^k, respectively. Here $\hat{\mathcal{L}}$ is a frequency response function

$$\hat{\mathcal{L}}(\epsilon, \tau, d_1, d_2, \cdots, d_m) = e^{-\left(\sum_{j=1}^{m} d_j (w^2)^j + \epsilon\right)\tau} + \frac{\epsilon}{\sum_{j=1}^{m} d_j (w^2)^j + \epsilon} \left(1 - e^{-\left(\sum_{j=1}^{m} d_j (w^2)^j + \epsilon\right)\tau}\right), \tag{2.11}$$

where $w^2 = \sum_{i=1}^{n} w_i^2$.

The solution algorithm developed in the above Fourier domain is called a fast PDE transform. In the present work, we explore the use of the fast PDE transform in the form of Eq. (2.10) for integrating hyperbolic conservation law systems.

To obtain a straightforward interpretation of the PDE transform (2.11), let us investigate the simple case in one dimension when $d_m = 1$ and $d_i = 0$, $(i = 1, \cdots, m-1)$ as well as $\epsilon = 0$ so that we can focus on the effect of leading order $2m$. Let $l = 2m$, then l denotes the order of PDE transform. We vary the order l and propagation time τ to study different PDE transforms.

Fig. 1(a) shows the frequency responses of the PDE transform for three different orders $l = 2, 10$ and 40, with the fixed propagation time of $\tau = 1$. In the figure, the y-axis gives the magnitude of the frequency response while the x-axis is the wavenumber in $[0, \pi]$. Here, the discrete points are sampled evenly from 128 wavenumbers over $[0, \pi]$.

From Fig. 1(a), one can observe that the 2nd-order PDE transform suffers from a long transition band and a short effective wavenumber region, i.e., the range of wavenumbers in which the frequency response is unit. As the order increases from 2 to 40, the frequency response decays from magnitude 1 to 0 more and more rapidly, leading to sharp transitions.

One can obtain a better understanding of the difference between the three PDE transforms in Fig. 1. We plot 5 frequency responses of the 2nd-order PDE transform with propagation time $\tau = 10^2$, 10^1, 10^0, 10^{-1} and 10^{-2} from left to right in Fig. 1(b). It is seen
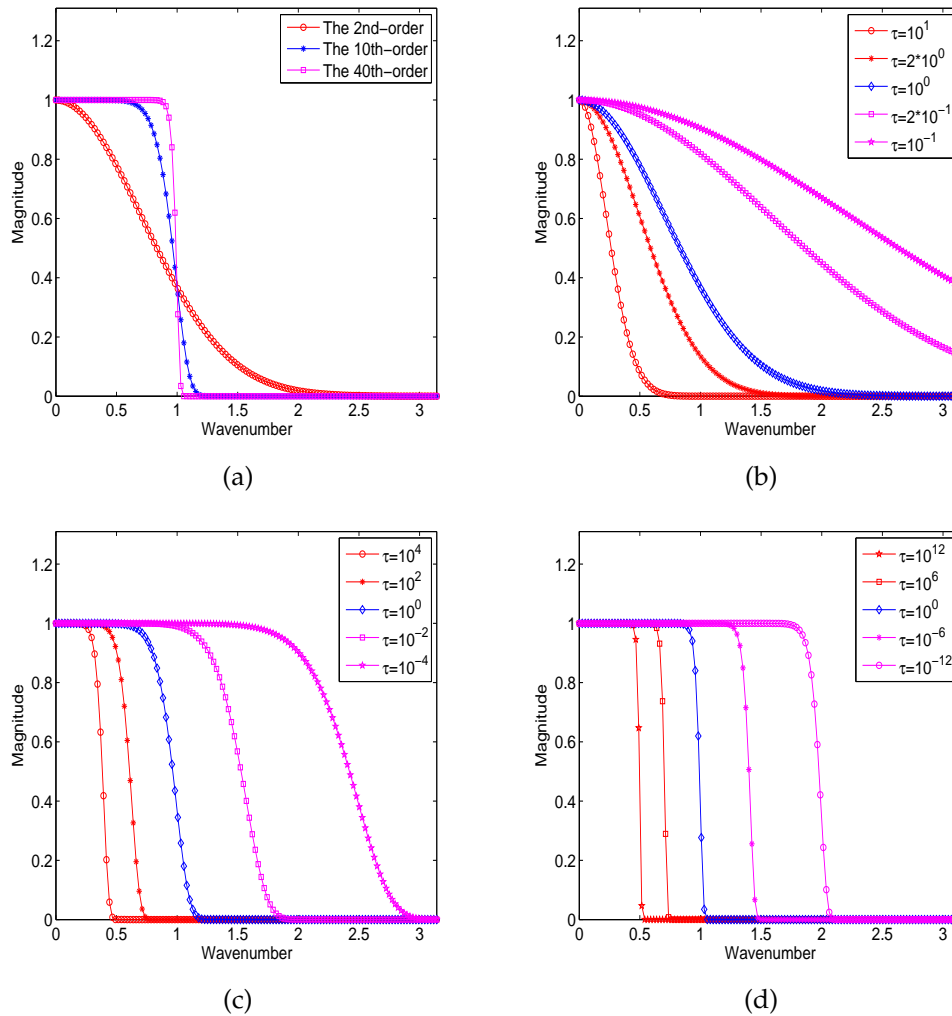
Figure 1: Frequency response of PDE transforms of different orders and propagation time. (a) Order $l=2$, 10 and 40 from left to right with $\tau=1$. (b) The 2nd-order: $\tau=10^1$, $2*10^0$, 10^0, $2*10^{-1}$ and 10^{-1} from left to right. (c) The 10th-order: $\tau=10^4$, 10^2, 10^0, 10^{-2} and 10^{-4} from left to right. (d) The 40th-order: $\tau=10^{12}$, 10^6, 10^0, 10^{-6} and 10^{-12} from left to right.

that the frequency responses with long propagation time $\tau=10^1, 2*10^0$ and 10^0 have a short low-pass region while frequency responses with small propagation time $\tau=2*10^{-1}$ and 10^{-1} preserve part of the high-frequency information. Fig. 1(c) illustrates 5 frequency responses of the 10th-order transform with propagation time $\tau=10^4$, 10^2, 10^0, 10^{-2} and 10^{-4} from left to right. It appears that the frequency response of 10th-order PDE transform gently damps from magnitude 1 to 0, which results in the property of compromising low-frequency and some high-frequency information. However, the 40th-order PDE

transform in Fig. 1(d) has a very sharp transition band, which is close to an ideal filter.

It can also be observed in Fig. 1 that the effective wavenumber region is adjustable by the propagation time τ. For a fixed order of the PDE transform, the shorter the propagation time τ, the longer the effective wavenumber region. Although the transition band of the PDE transform with shorter propagation time is relatively wider than that of long propagation time, the sharpness of transition is primitively dominant by the order of PDE transform as seen from Figs. 1(b), (c) and (d).

The comparison of the above 2nd-, 10th-, and 40th- order PDE transforms provides us a highlight of the different characteristics for the low, high and very high order PDE transforms. For the practical application of PDE transform design, since the order l of the PDE transform vary from small to large positive even number, it is subtle to choose an appropriate order of the PDE transform to resolve various problems. In general, high order PDE transforms, such as order 40, 50, and higher, are very valuable in mode decomposition of signals [47, 49]; while PDE transforms of intermediate orders, i.e., 6, 8 and 10, are suitable for the surface construction of biomolecules [60]; yet low order PDE transforms, such as orders 2 and 4, are quite robust for many common tasks in image analysis [47,49]. Due to the complexity of hyperbolic conservation laws, it takes the PDE transforms of a variety of orders for shock capturing. This aspect is thoroughly investigated in the present work.

2.3　Numerical algorithm

In the present algorithm for integrating hyperbolic conservation laws, the time integration is implemented via the 4th order Runge-Kutta scheme, which utilizes 4 spatial integrations to update each time. At a given physical time step, spatial integrations are carried out in the frequency domain via the Fourier pseudospectral method. For each spatial integration, we just perform at most one iteration of the PDE transform, depending on the need. In fact, when this iteration is implemented in the Fourier pseudospectral method (frequency-domain), it is actually incorporated into the Fourier transform or the weighted Fourier transform. As such, we just need to modified the Fourier transform coefficient without performing the one-iteration PDE transform separately.

Specifically, we apply the PDE transform to systems of hyperbolic conservation laws via the following two-step procedure:

$$\bar{U}^{k+1} = \mathcal{B} U^k, \tag{2.12}$$

$$U^{k+1} = \mathcal{L} \bar{U}^{k+1}, \tag{2.13}$$

where the operator $\mathcal{B}$ in Eq. (2.12) is the basic time integration from time k to time $k+1$ and the operator $\mathcal{L}$ in Eq. (2.13) is a possible application of the PDE transform. Here, U^k and U^{k+1} is the numerical solution of u in Eq. (1.1) at time step k and $k+1$, respectively, while $\bar{U}^{k+1}$ is the intermediate numerical solution of u after implementing operator $\mathcal{B}$ on U^k.

The operator $\mathcal{B}$ in Eq. (2.12) can be defined by a general numerical method for the time evolution. Here, we use the fourth-order Runge-Kutta scheme. The FPM is utilized for the spatial discretization of $f(u)_x$ in the frequency domain.

In specific, after carrying out the fast Fourier transform on f, we obtain the frequency response $\widehat{f}$, i.e. $\widehat{f} = FFT(f)$. Then $i\omega\widehat{f}(\omega)$ is the frequency response of f_x, where $i = \sqrt{-1}$ is the imaginary root. By doing the inverse fast Fourier transform on $i\omega\widehat{f}(\omega)$, we obtain the spatial discretization of $f(u)_x$ as $IFFT(i\omega\widehat{f}(\omega))$.

For simple and continuous problems, scheme (2.12) works well. However, for hyperbolic conservation systems involving discontinuity, the accumulation of Gibbs' oscillations as time evolves may result in spurious solutions or even numerical blow ups. Thus, we make use of PDE transform [40] to eliminate the possible Gibbs' oscillations from basic time integration (2.12). The application of the PDE transform is controlled (i.e., turned on or turned off) by an adaptive sensor. The sensor is characterized by a measure of high frequency denoted by $\|\mu\|$ and regulated by a threshold value η. Once the increment in high frequency measure, $\Delta\mu$, exceeds the threshold η, the PDE transform in Eq. (2.13) is implemented. In our test, we apply a straightforward high frequency measure $\|M\|$ as the TVD sensor, which is defined by

$$\left\| \mu(\bar{U}^{k+1}) \right\| = \sum_i \left| \bar{U}_{i+1}^{k+1} - \bar{U}_i^{k+1} \right|, \tag{2.14}$$

where $\bar{U}_i^{k+1}$ and $\bar{U}_{i+1}^{k+1}$ denote the intermediate numerical solution of u at time $k+1$ on spatial point i and $i+1$, respectively, while $\|\mu(\bar{U}^{k+1})\|$ is the total variation measure of $\bar{U}^{k+1}$. As a result, by checking whether the increment of high frequency $\Delta\mu(\bar{U}^k) = \|\mu(\bar{U}^{k+1})\| - \|\mu(\bar{U}^k)\|$ exceeds η or not, we can decide whether to apply the PDE transform.

Eq. (2.13) in the second step is given by the PDE transform to suppress Gibbs' oscillations. We implement the PDE transform in frequency domain, which results in

$$\hat{U}^{k+1} = \hat{\mathcal{L}}\hat{\bar{U}}^{k+1}, \tag{2.15}$$

where $\hat{U}^{k+1}$ and $\hat{\bar{U}}^{k+1}$ are the frequency responses of U^{k+1} and $\bar{U}^{k+1}$ respectively, while $\hat{\mathcal{L}}$ is defined in Eq. (2.11). In this work, we adopt the simple implementation of PDE transforms of $d_m = 1$ and $d_i = 0$, $(i=1,\cdots,m-1)$ as well as $\epsilon = 0$, as mentioned before. As a result, the design of the PDE transform depends on the highest order of $l = 2m$ and propagation time τ, whose properties have been analyzed in the last section.

It should be noted that the implementation of the Fourier pseudospectral method demands periodic boundary condition. However, there are often non-periodic boundary condition in practical applications. We handle the non-periodic computation domain by symmetrically extending it to the auxiliary domain. This approach works well as shown in our previous work [40]. In specific, the symmetrical extension of the computation domain in 1D is in the following scheme. Suppose the original domain is discretized by $N+1$ grid points indicated by $i = 1,\cdots,N+1$, then the computation domain is doubled

with $2N$ grid points and $f(u)$ and u are extended by

$$\{f(u)\}_i = \{f(u)\}_{2N+2-i}, \quad i = N+2, \cdots, 2N, \tag{2.16}$$

$$\{u\}_i = \{u\}_{2N+2-i}, \qquad\quad i = N+2, \cdots, 2N, \tag{2.17}$$

where $\{\cdot\}_i$ corresponds to the value at the ith pixel. This extending procedure is straight-forward to apply to 2D and 3D dimension.

After the entire time integration has been completed, we adopt a cosmetic post-processing filter as introduced by Gottlieb *et al.* [14] to make the solution more presentable. In our numerical experiments, we employ the Lagrange-4 as the post processing filter. The reader is referred to our earlier work [41] for its implementation detail.

3 Numerical tests and validation

The performance of the proposed PDE transform on the solution of hyperbolic conservation law systems is validated through test examples in this section. A number of standard linear and nonlinear benchmark problems are studied in the present work, from scalar conservation law systems including the linear advection equation, Burgers' equation and problem with non-convex flux, to one dimensional (1D) and two dimensional (2D) Euler equations, including shock tube (Sod's and Lax's) problems, 1D and 2D shock-entropy interaction, as well as 2D shock-vortex interaction.

The proposed PDE transform can be applied directly on those problem with periodic boundary conditions. However, for non-periodic boundary conditions, the computation domain is symmetrically doubled to convert to a periodic one.

The problems which involves in the non-periodic boundary conditions are Example 3 (Inviscid Burgers' equation), Example 4 (Non-convex flux), Example 5 (Sod's and Lax's problems), Example 6 (1D Shock-entropy interaction), Example 7 (Shu-Osher's problem), Example 8 (2D Shock-entropy interaction) and Example 9 (2D Shock-vortex interaction).

It is noted that the selection of order $l = 2m$ and propagation time τ of the PDE transform is quite sophisticated. On the one hand, the order should not be too high, while the propagation time should not be too small. Otherwise, the PDE transform has little effect in suppressing the Gibbs' oscillation of the solution. On the other hand, the order should not be too low, while the propagation time should not be too large. Otherwise, they result in too much dissipation. Owing to diversity of hyperbolic conservation law systems, the best choices of order and propagation time are problem dependent, which are listed in the table in Appendix.

It is noted that both the PDE transform and hyperbolic conservation law systems are time dependent. To avoid possible confusion, we denote "τ" as the propagation time of the PDE transform and designate "t" as evolution time of the conservation law system in the rest of the paper.

3.1 Scalar conservation law systems

We first consider 1D scalar conservation law systems, whose governing equation is expressed in the form of

$$u_t + f(u)_x = 0, \tag{3.1}$$

with $f(u)$ as a function of u. Three types of $f(u)$, including $f(u) = u$ and convex flux $\frac{1}{2}u^2$ as well as non-convex flux $\frac{1}{4}(u^2-1)(u^2-4)$, are studied in the present work.

3.1.1 Example 1 (Linear advection equation with Sine-Gaussian wavepacket)

The first test example is the linear advection equation given by

$$\begin{aligned}
u_t + cu_x &= 0, \quad -1 < x < 1, \\
u(x,0) &= u_0(x), \quad \text{periodic},
\end{aligned} \tag{3.2}$$

where $u_0(x)$ is the initial value. We set $u_0(x)$ as [62]

$$u_0(x) = \sin[2\pi\kappa(x-x_0)]e^{-\frac{(x-x_0)^2}{2\sigma^2}}, \tag{3.3}$$

where the parameter of wavenumber κ can be tuned to produce highly oscillatory wavepacket, x_0 is the initial location of wavepacket center and σ is a constant regularizing the width of the wave packet. We set $x_0 = 0$ and $\sigma = \sqrt{2}/10$ such that the tail of wavepacket is constrained over the computation domain $[-1,1]$. It is straightforward to show that the exact solution is given by $u(x,t) = u_0(x-t)$, which is a translation of the initial solution at a unit speed, resulting in the fact that the initial wavepacket repeats itself every two time units over the computation domain $[-1,1]$. The mesh size is chosen as $N = 128$ to implement the PDE transform while the time increment is selected as small as 10^{-4} to ensure that the time discretization error is negligible.

We vary wavenumber κ to explore the accuracy and stability of the PDE transform strategy for the wavepacket propagation. For low frequency waves, a low-order method can work well to obtain accurate solutions. However, as the wavenumber κ increases, the wavepacket becomes more and more oscillatory. It is challenging for low resolution schemes to resolve the highly oscillatory advective wavepacket. Therefore, one needs to resort to a high order method. In our test, we apply the 6th-order PDE transform for low frequency wavepackets, i.e., $\kappa = 5$ and 10, and 12th-order PDE transform for high frequency wavepackets, i.e., $\kappa = 20$ and 25.

Figs. 2(a), (b) and (c) show the computational results and exact solutions at time $t = 100$ for three different frequencies $\kappa = 5, 10$ and 20. It is obvious that there is no visual difference between the numerical and exact solutions in Figs. 2(a) and (b). However, for the case of $\kappa = 20$, the solution does not show the peaks and valleys of the exact wavepacket. One may regard the solution as being imperfect. In fact, this is not true. The L_∞ error listed in Table 1, is as small as 2.67E-6. Therefore the numerical solution is extremely
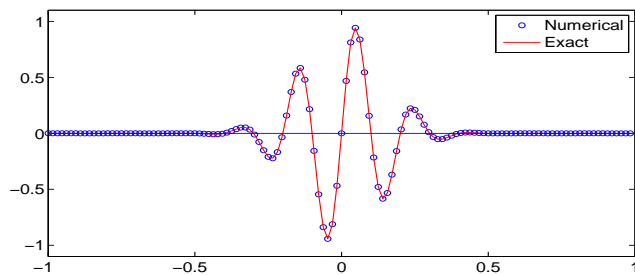
(a) $\kappa = 5$, $N = 128$
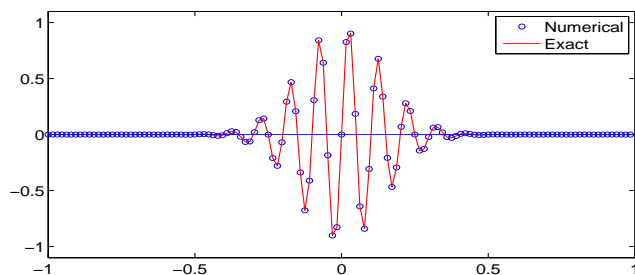
(b) $\kappa = 10$, $N = 128$
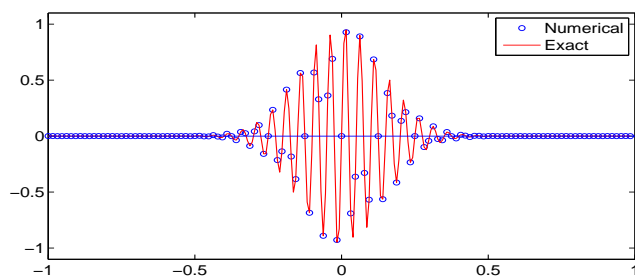
(c) $\kappa = 20$, $N = 128$, before the interpolation
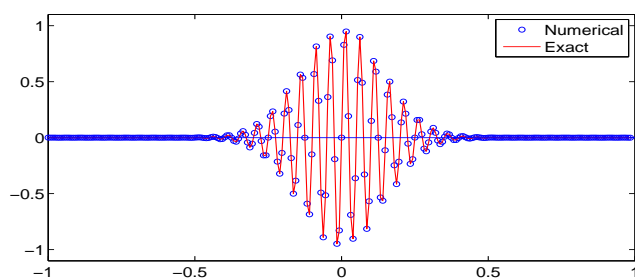
(d) $\kappa = 20$, $N = 128$, after the interpolation

Figure 2: Results from the PDE transform for the advection equation with the Sine-Gaussian wave packet ($t = 100$, $\Delta t = 10^{-4}$).

accurate. The truth is that, because so few grid points are used in our computation, there are not enough grid points to fully represent the wavepacket. Nevertheless, the origin information of the wavepacket is perfectly built in the solution. To illustrate this point, we interpolate the present solution to a denser grid ($N = 256$) as shown in Fig. 2(d) by using our DSC algorithm [46, 50, 56]. Indeed, we are able to fully restore all extrema in the wavepacket based on the information presented in Fig. 2(c). This confirms that our scheme is still able to perform well for high frequency waves under a very small ratio of grid points over wavelength.

It is also meaningful to check the long time integration of the numerical method. Table 1 lists the numerical L_∞-error from $t = 10$ to $t = 100$. One can tell that the numerical errors are under good control during the time integration. As a comparison, we also list in Table 1 the results of a CFOR-Hermite method proposed in our earlier work [62]. The CFOR-Hermite method is based on the local spectral wavelet approach for the spatial discretization and the conjugate filter method for oscillation reduction. It has been intensively validated for solving the Navier-Stokes equation and integrating conservation law systems [62].

In the work of [62], the CFOR-Hermite method employs 100 points but takes the same time step $\Delta t = 10^{-4}$. From Table 1, one can notice that the errors from the PDE transform is slightly smaller than those from the CFOR-Hermite method. We are quite confident that the results listed in Table 1 are some of the best when $\kappa = 25$. It can be concluded that the numerical accuracy and long time stability are well resolved by the proposed PDE transform.

The time step size of $\Delta t = 10^{-4}$ is quite small. In fact, we can increase the time step size to enhance the efficiency. However, larger time step size will sacrifice the accuracy. Table 2 shows that the 4th order converges in the L_∞ error. This result is consistent with the fact that we use the 4th order Runge-Kutta algorithm.

Table 1: L_∞ error for long-time integration of the Sine-Gaussian wavepacket.

Time		10	20	50	80	100
PDE transform	$\kappa = 20$	2.69E-7	5.38E-7	1.34E-6	2.15E-6	2.67E-6
	$\kappa = 25$	8.10E-7	1.62E-6	4.06E-6	6.50E-6	8.47E-6
CFOR-Hermite	$\kappa = 20$	2.78E-7	5.56E-7	1.39E-6	2.22E-6	2.78E-6
	$\kappa = 25$	1.51E-6	3.02E-6	7.55E-6	1.21E-5	1.51E-5

Table 2: L_∞ errors w.r.t. different time step sizes for the integration of the Sine-Gaussian wavepacket. ($t = 2$, $\kappa = 20$).

Δt	L^∞ error	order
10.0E-4	1.3E-4	
5.0E-4	8.1E-6	4.0
1.0E-4	1.3E-8	4.0

3.1.2 Example 2 (Linear advection equation with wave combination)

Another example is also a linear advection equation given by [23]

$$u_t + u_x = 0, \qquad -1 < x < 1,$$
$$u(x,0) = u_0(x), \quad \text{periodic}, \tag{3.4}$$

where $u_0(x)$ is the initial value given by

$$u_0(x) = \begin{cases} \frac{1}{6}\big(G(x,\beta,z-\delta)+G(x,\beta,z+\delta)+4G(x,\beta,z)\big), & -0.8 \le x \le -0.6, \\ 1, & -0.4 \le x \le -0.2, \\ 1-|10(x-0.1)|, & 0 \le x \le 0.2, \\ \frac{1}{6}\big(H(x,\alpha,a-\delta)+H(x,\alpha,a+\delta)+4H(x,\alpha,a)\big), & 0.4 \le x \le 0.6, \\ 0, & \text{otherwise.} \end{cases} \tag{3.5}$$

The functions G and H are set as

$$G(x,\beta,z) = e^{-\beta(x-z)^2},$$
$$H(x,\alpha,a) = \sqrt{\max(1-\alpha^2(x-a)^2,0)}, \tag{3.6}$$

where $z = -0.7$, $\delta = 0.005$, $\beta = \log 2/(36\delta^2)$, $a = -0.5$, and $\alpha = 10$.

The initial value of this problem is a smooth but narrow combination of a Gaussian, a square wave, a sharp triangle wave and a half ellipse. It is easy to show that the exact solution is given by $u(x,t) = u_0(x-t)$, which is a translation of the initial solution at a unit speed. It is well known that due to the contact discontinuity, the propagation by the linear advection equation leads to unphysical Gibbs' oscillations which may be induced by exponentially small numerical errors and their subsequent amplification. In Fig. 3, the numerical results obtained by using the PDE transform of second and eighth orders are demonstrated at $t = 8$ with 256 grid points. In fact, results for fourth and sixth orders, which are omitted to save the space, are very similar to those of second and eighth orders. The L_∞ errors for the second, fourth, sixth eighth order approaches are all below 0.01. It is interesting to observe that for this simple problem, not only the second order PDE transform works well, but also many higher order PDE transforms are able to produce satisfactory results.

In the above scheme, the time step size is set as $\Delta t = 0.001$. We can also use a larger time step size to enhance the efficiency. One attributes to measure the efficiency of the scheme is the CFL number. A larger time step size gives a higher CFL number. Fig. 4 shows the results for larger time step sizes $\Delta t = 0.002$ and $\Delta t = 0.004$, where it is seen that Gibbs oscillations are well suppressed. Our results indicate that PDE transform can also achieve high efficiency in suppressing Gibbs oscillations.

3.1.3 Example 3 (Inviscid Burgers' equation)

In this example, we test the performance of the present PDE transform for the most classical model, inviscid Burgers' equation with convex flux $f(u) = u^2/2$ and Riemann type of initial conditions with constant u_l on the left and u_r on the right.

(a) The 2nd-order

(b) The 8th-order
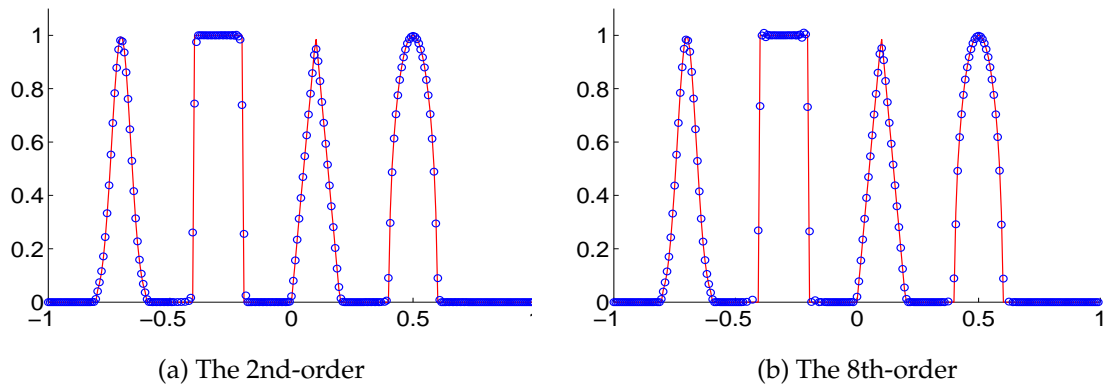
Figure 3: Results from the PDE transform of various orders for the advection equation ($t=8,\Delta t=0.001$, 256 grid points).

(a) $\Delta t=0.002$, CFL$=0.25$

(b) $\Delta t=0.004$, CFL$=0.5$
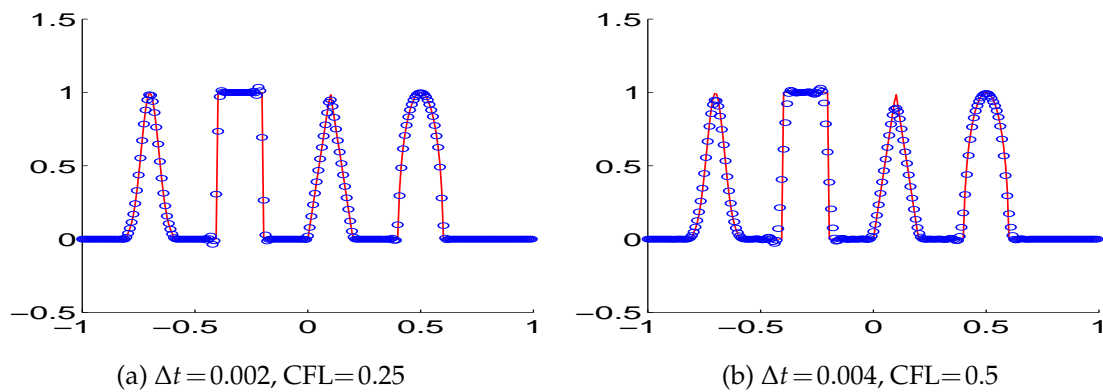
Figure 4: Results from the PDE transform with larger time step sizes for the advection equation ($t=8$, 256 grid points).

(3a) First we consider the Riemann initial value with $u_l > u_r$ as

$$u(x,0)=\begin{cases} u_l=1, & x\leq 0, \\ u_r=0, & x>0. \end{cases} \tag{3.7}$$

This problem has been studied by numerous researchers because it is a standard benchmark problem in hyperbolic conservation laws. The exact solution is given by a shock wave with a constant velocity σ, i.e.

$$u(x,t)=\begin{cases} u_l, & \frac{x}{t}<\sigma, \\ u_r, & \frac{x}{t}>\sigma, \end{cases} \tag{3.8}$$

where

$$\sigma=\frac{f(u_l)-f(u_r)}{u_l-u_r}=\frac{1}{2}.$$
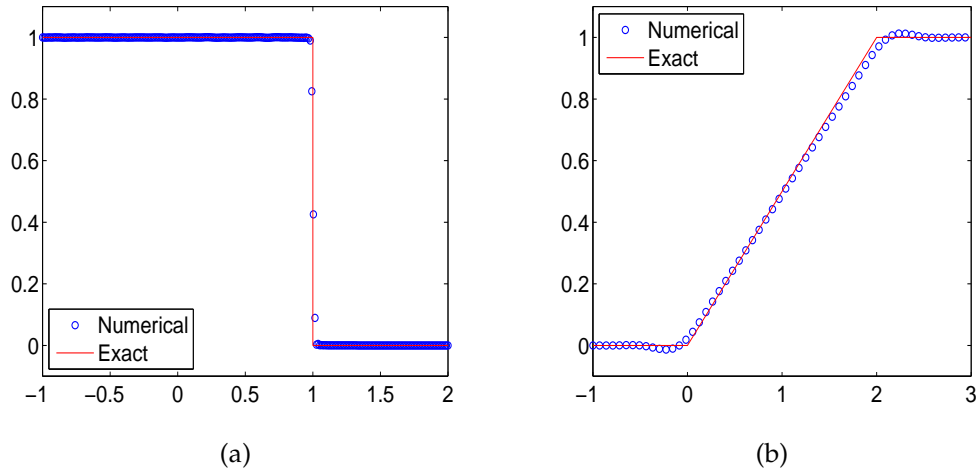
Figure 5: Results from the 6th-order PDE transform for the inviscid Burgers' equation at time $t=2$. (a) $u_l=1$, $u_r=0$, 257 grid points; (b) $u_l=0$, $u_r=1$, 129 grid points.

It is observed that this problem has a non-periodic boundary condition. Consequently, the computational domain needs to be symmetrically doubled in the x-direction to obtain periodic boundary condition when applying the Fourier pseudospectral method [40] pairing with the PDE transform. Since the initial condition is piecewise constant and exact solution does not involve large oscillation, a low-order scheme is suitable to render a satisfactory numerical solution. In this case, we apply second, fourth and sixth order PDE transforms to resolve the problem. The numerical results from the sixth order PDE transform are plotted in Fig. 5(a) at time $t=2$. It is demonstrated that the Gibbs' oscillation is well resolved and the shock front, which moves to $x=1$, is well captured. Although this problem prefers low order shock-capturing methods [23], it is concluded that the PDE transform based FPM method works well for this problem too.

(3b) As another example, we check the present method by using the Riemann type initial value with $u_l < u_r$ as

$$u(x,0)=\begin{cases} u_l=0, & x<0, \\ u_r=1, & x\geq 0. \end{cases} \tag{3.9}$$

The exact solution is given by a rarefaction wave

$$u(x,t)=\begin{cases} 0, & \frac{x}{t}<f'(u_l), \\ G(\frac{x}{t}), & f'(u_l)<\frac{x}{t}<f'(u_r), \\ 1, & f'(u_r)<\frac{x}{t}, \end{cases} \tag{3.10}$$

with $f'(u_l)=u_l$, $f'(u_r)=u_r$ and $G(x/t)=(f')^{-1}(x/t)=x/t$.

Similar to Case (3a), the computational domain is symmetrically doubled in the x-direction to obtain periodic boundary condition before applying the PDE transform and

FPM. Furthermore, the piecewise constant initial condition and exact solution imply that this problem can be well resolved by a low-order shock-capturing scheme. In our approach, we apply the sixth order PDE transform, paired with the FPM, to solve the equation. The numerical results from the sixth order PDE transform are plotted in Fig. 5(b) at time $t=2$. From the figure, it is seen that the rarefaction fan over [0,2] is free of oscillation. The feature of the solution is well resolved.

3.1.4 Example 4 (Non-convex flux)

. We next consider a problem with a non-convex flux to test the convergence to the physically correct solution. The non-convex flux is given by

$$f(u) = \frac{1}{4}(u^2 - 1)(u^2 - 4) \tag{3.11}$$

with a Riemann initial condition

$$u(x,0) = \begin{cases} u_l = -3, & x < 0, \\ u_r = 3, & x \geq 0. \end{cases} \tag{3.12}$$

The exact solution is given by

$$u(x,t) = \begin{cases} u_l, & \frac{x}{t} \leq f'(u_l), \\ G(\frac{x}{t}), & f'(u_l) < \frac{x}{t} < 0, \\ -G(-\frac{x}{t}), & 0 < \frac{x}{t} < f'(u_r), \\ u_r, & f'(u_r) \leq \frac{x}{t}, \end{cases} \tag{3.13}$$

with $f'(u_l) = -19.5$, $f'(u_r) = 19.5$ and $G(u)$ is the solution of $f'(G(u)) = u$ in the convex part of f, which is $|u| > \sqrt{5/6}$. It should be noted that the solution is discontinuous at $x=0$ and $G(0) = \sqrt{2.5}$.

The exact solution and more detailed information about this problem are given in [20]. This problem is relatively more complicated than the convex flux case. In the literature, commonly reported numerical result is at $t = 0.04$ [23]. The numerical results of the PDE transform are showed in Figs. 6(a) and (c). It is seen that the shock front at $x = 0$ is almost exactly captured. Particularly, there is no numerical solution point located on the discontinuity.

As a comparison, we consider the Fourier pseudospectral method (FPM) with the regularized Shannon kernel (RSK) approach, which was extensively validated in our earlier work [40]. In Figs. 6(b) and (d), this approach is labeled as FPM-RSK. It is obvious that compared with the FPM-RSK, the present PDE transform yields a more satisfactory resolution. We believe that our results from the PDE transform based FPM approach are some of the best ever reported for this classic problem.

(a) The 4th order PDE transform (129 grid points)

(b) FPM-RSK (129 grid points)

(c) The 6th order PDE transform (65 grid points)

(d) FPM-RSK (65 grid points)
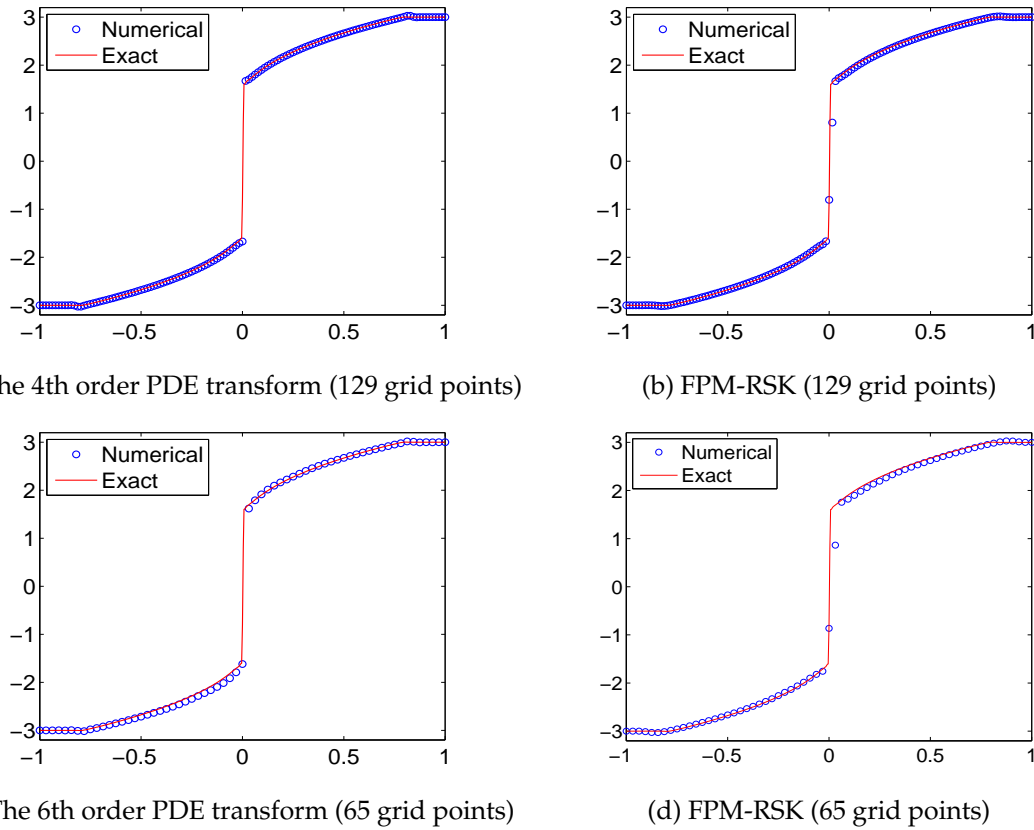
Figure 6: Comparison between numerical results from the PDE transform and FPM-RSK method for the problem with a non-convex flux ($t=0.04$, $\Delta t=0.0005$).

3.2 1D Euler systems

In this subsection, we carry out numerical experiments by using the proposed PDE transform scheme for the 1D Euler equation of gas dynamics. In one dimension, the Euler equation takes the form [23, 40]

$$U_t + F(U)_x = 0 \tag{3.14}$$

with

$$U = \begin{pmatrix} \rho \\ \rho u \\ E \end{pmatrix}, \qquad F(U) = \begin{pmatrix} \rho \\ \rho u \\ E \end{pmatrix} u + \begin{pmatrix} 0 \\ p \\ pu \end{pmatrix}, \tag{3.15}$$

where ρ, u, p and E denote the density, velocity, pressure and total energy per unit mass

$$E = \rho \left[e + \frac{1}{2} u^2 \right], \tag{3.16}$$

respectively. Here, e is the specific internal energy. For an ideal gas with the constant specific heat ratio ($\gamma = 1.4$) considered here, one has

$$e \;=\; \frac{p}{(\gamma-1)\rho}. \tag{3.17}$$

In the following, we consider two well-known Riemann problems.

3.2.1 Example 5 (Sod's and Lax's problems)

Here we apply the PDE transform based FPM on two shock tube problems, i.e., Sod's problem and Lax's problem, which are both standard benchmark tests. In fact, due to their simple profiles, these problems favor low order schemes.

Sod's problem is a special case of shock tube problem with velocities on both sides of the discontinuity being set to zero. It is often used as a test case for validation of numerical shock capturing schemes, because analytical solutions are available. The initial condition for Sod's problem is given by

$$(\rho,u,p)_{t=0} = \begin{cases} (1,0,1), & x<0, \\ (0.125,0,0.1), & x \geq 0; \end{cases} \tag{3.18}$$

while the initial condition for Lax's problem is given by

$$(\rho,u,p)_{t=0} = \begin{cases} (0.445,0.698,3.528), & x<0, \\ (0.5,0,0.571), & x \geq 0. \end{cases} \tag{3.19}$$

Although there are coupled equations in the system, which make it more complicated than scalar equations, the Sod and Lax problems involve multiple piecewise constant solution without much oscillation. Therefore, these problems favor low-order numerical methods. In our study, we utilize the 6th-order PDE transform method with the FPM to integrate these shock tube equations. Our results of density and pressure for Sod's problem are depicted in Fig. 7. It is perceived that three characteristics of Sod's problem, including the rarefaction wave, the contact discontinuity and the shock discontinuity are well resolved and captured.

Figs. 8(a) and (b) illustrate the present numerical results for Lax's problem. Similar to the Sod's case, three characteristics of Lax's problem, including the rarefaction wave, the contact discontinuity and the shock discontinuity are also well captured. It can be seen that the present method gives a good resolution in both cases.

As a comparison, we plot the results obtained by the FPM-RSK approach [40] in Figs. 8(c) and (d). As discussed earlier, the FPM-RSK scheme is a robust approach for hyperbolic conservation laws. It is seen from Fig. 8 that the present PDE transform performs at least as good as, if it is not better than, the FPM-RSK approach for shock tube problems.

All of the preceding test examples, except for the high-frequency case in Example 1, favor low order shock capturing schemes. In such a case, although the present method,
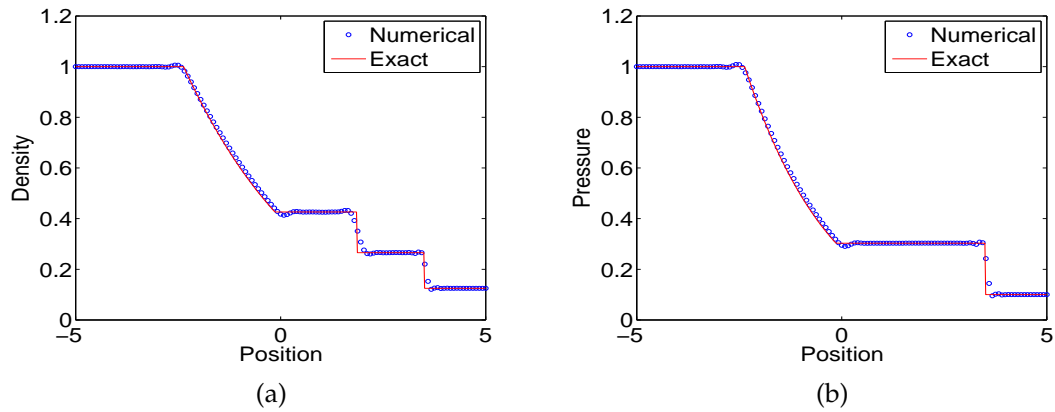
Figure 7: Numerical results from the 6th-order PDE transform for Sod's problem ($t=1.5$, $\Delta t = 0.02$, 129 grid points). (a) Density; (b) Pressure.
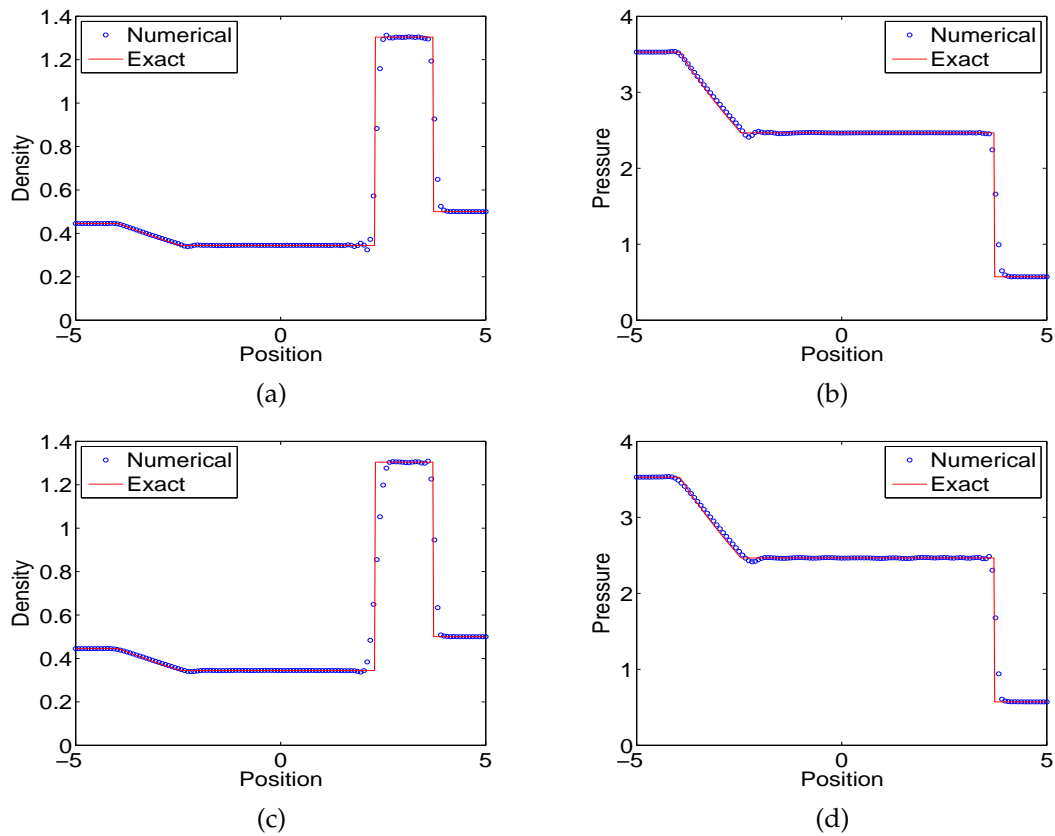
Figure 8: Comparison of numerical results from the 6th-order PDE transform and the FPM-RSK for Lax's problem ($t=1.5$, $\Delta t = 0.02$, 129 grid points). (a) Density from the PDE transform; (b) Pressure from the PDE transform; (c) Density from the FPM-RSK; (d) Pressure from the FPM-RSK.

as well as other high-order shock capturing schemes, work extremely well, it does not have a cutting edge advantage over low order methods. In the next three examples, we consider a class of problems that require high-order shock capturing methods for efficient spatial discretizations. Whereas, it will be extremely difficult, if it is not impossible, for low order methods to resolve this class of problems.

3.2.2 Example 6 (1D Shock-entropy interaction)

The interaction between a Mach 3 right-moving shock and an entropy wave of small amplitude in a one-dimensional flow, which is a standard test problem [18, 23, 40], is investigated in this example. This problem is important because of its relevance to the interaction of shock and turbulence. We take the computation domain over [0,9] and initialize the flow field with

$$(\rho, u, p)_{t=0} = \begin{cases} (3.85714, 2.629369, 10.33333), & x < 0.5, \\ (e^{-\epsilon \sin(\kappa x)}, 0, 1.0), & x \geq 0.5. \end{cases} \tag{3.20}$$

The parameters ϵ and κ are the amplitude and the wave number of the entropy wave before the shock. In this numerical experiment, the small amplitude of the pre-shock entropy is kept the same, i.e. $\epsilon = 0.01$ while the wave number κ is varied. The amplitude of the amplified wave after the shock can be given by linear analysis [33], which is a constant of 0.08690716.

This problem of shock and entropy interaction becomes more and more challenging as the frequency κ increases. The difficulty lies in the fact that it is hard to distinguish the amplified high frequency entropy wave from the spurious oscillations. Low order numerical schemes may dramatically damp the amplitude of the transmitted high frequency wave. Even some high order schemes encounter the same numerical difficulty. A satisfactory numerical scheme should possess the quality of suppressing Gibbs' oscillation while preserving amplitude of the entropy wave as well as capturing the shock [18, 23, 40].

In our numerical test, the shock is set to move from $x = 0.5$ to $x = 8.5$. For the convenience of a comparison with previous results, we only display the results at interval [3.0, 9.0]. Furthermore, for the purpose of discharge transient waves due to the non-numerical initial shock profile, we plot the length of the amplified entropy waves in the same manner as that in Ref. [23]. Additionally, we would like to point out two nontrivial details in the illustration. The first one is that the plotted results are obtained by an interpolation of our final numerical results from a coarse grid to a denser grid, which has already been adopted for plotting the high-frequency Sine-Gaussian wavepacket in Example 1. This is necessary because our computational grid is too coarse to show all the peaks and valleys of our numerical results. The second one is that a post processing filter, which was discussed in Section 2.3, is employed to eliminate the oscillations near the shock when we present the final result after the completion of the entire time integration.

First, we test the shock capture for a case with relatively low frequency $\kappa = 18$. We set 513 grid points over the computation domain [0,9] to implement the PDE transform cou-

pled with the Fourier pseudospectral method. It is difficult for a low-resolution method, such as a first order or a second order shock capturing method to preserve the amplitude of high-frequency entropy wave and suppress oscillation [23].

In our numerical test study, we found that the low-order PDE transform does not work well for this problems, although the FPM is employed. Low order PDE transforms either damp the amplitude of the high-frequency entropy wave or cannot suppress Gibbs' oscillations. In contrast, we found that a moderately high order PDE transforms with suitable propagation time perform much better. Fig. 9(a) shows the amplitude of the shock entropy of $\kappa = 18$ obtained by using the 12th-order PDE transform. It can be seen that the entropy waves almost fully span two strips bounded by two analytical solid lines $y = 0.08690716$ and $y = -0.08690716$, which indicates that the amplitude of amplified wave is well preserved. As the amplified entropy wave is monochromic post the shock, it is appropriate to characterize the resolution of the present method by points per wavelength (PPW). A further simple calculation on the amplified entropy wave tells that the resolution is about 5.3 PPW, which is among the best results for this shock entropy problem, to our best knowledge.

Next we increase the frequency to $\kappa = 32$. As there are many more amplified entropy wave post the shock, it is difficult to use 513 grid points to maintain the amplitude of high-frequency wave post shock. Instead, we deploy a mesh of 1025 grid points so as to render a better result. In this case, we still employ a 12th-order PDE transform but with a different propagation time from $\kappa = 18$. One still needs to be careful to design an appropriate PDE transform for this more complicated problem. Fig. 9(b) shows the amplitude of the shock entropy wave of $\kappa = 32$ by a 12th-order PDE transform. It is perceived that the entropy wave is still able to almost fully span two strips bounded by two solid lines $y = 0.08690716$ and $y = -0.08690716$. Furthermore, the waves at shock front are free of oscillation.

Finally, we consider a more challenging situation by setting a larger κ. We use 2049 grid points in our spatial discretization of the computation domain $[0,9]$. Fig. 9(c) presents the result of the case for $\kappa = 60$. It is clear that the waves post shock are well preserved while the waves at shock front are free of oscillation and well maintained. It also worthwhile to mention that the resolution for this case is about 5.9 PPW, which is still the best record at such a high κ value to our knowledge. Our results indicate that the present PDE transform is able to distinguish the high-frequency entropy waves from spurious oscillation. The above test cases of different frequencies imply that the PDE transform can be a powerful tool for solving hyperbolic conservation law systems involving the interaction of shock and high frequency entropy waves.

As stated earlier, low order shock capturing schemes will encounter difficulties for the above test cases. In fact, not all PDE transforms are suitable for these problems. The inappropriate selections of the PDE transform will either pollute the amplitude of entropy waves or cannot suppress the oscillation. We illustrate this point by using the setting of $\kappa = 32$ and 1025 grid points. Fig. 10(a) demonstrates the result from a 6th-order PDE transform, which illustrates the effect of a low order PDE transform. Although the waves
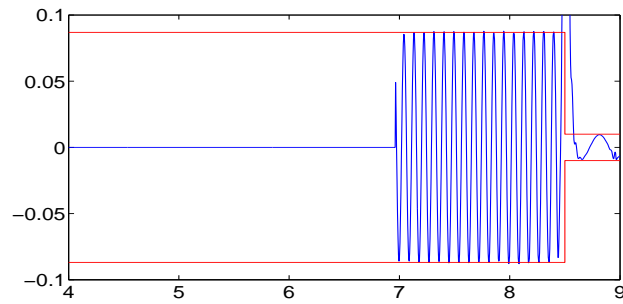
(a) $\kappa = 18$
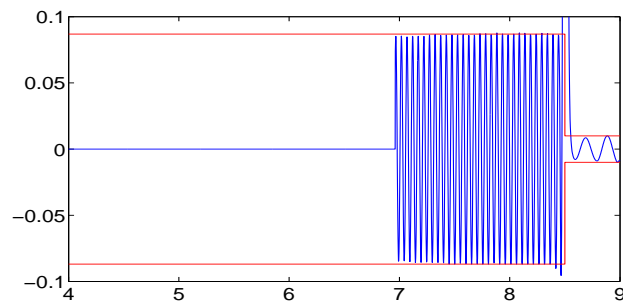
(b) $\kappa = 32$
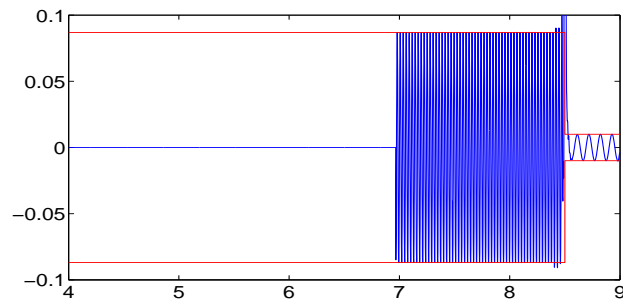
(c) $\kappa = 60$

Figure 9: The amplitude of entropy waves in the 1D shock-entropy interaction problem for different frequencies resulting from the 12th-order PDE transform.

in the shock front is perfectly kept, the amplitude of the entropy waves post shock is severely damped. We found that second order and fourth order PDE transforms perform even worse for this problem. As another check, we would like to investigate the performance of a very high order PDE transform for this problem. Although a high order PDE transform works well in preserving the high-frequency entropy waves post the shock, it may also pollute the relatively low frequency waves in the shock front. Fig. 10(b) shows the result from a 40th-order PDE transform. It is clear that the entropy waves in the shock front are polluted by Gibbs' oscillations.

(a)

(b)
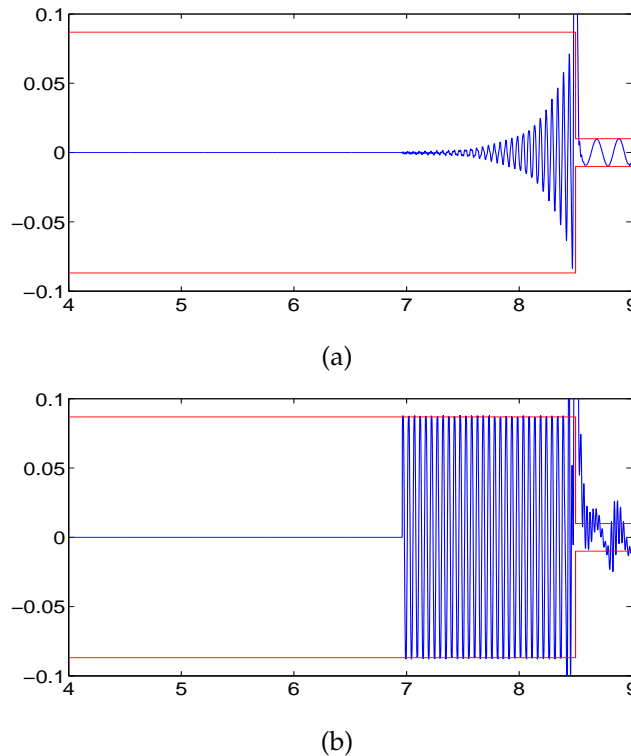
Figure 10: The amplitude of entropy waves in the 1D shock-entropy interaction problem for $\kappa = 32$ resulting from PDE transforms of low and extremely high-order. (a) The 6th-order PDE transform; (b) The 40th-order PDE transform.

3.2.3   Example 7 (Shu-Osher's problem)

We now examine the performance of the PDE transform on the problem of Shu and Osher, which is another typical case to test the capability of a numerical method in predicting shock/entropy interactions. This problem is also initialized by a Mach 3 right-moving shock and an entropy wave, which is in the sine form. Compared with the last problem, Shu and Osher problem involves many different frequencies. It is relatively difficult for low order numerical methods.

We consider the computational domain of $[-1,1]$ with flow field initialized by

$$(\rho,u,p)_{t=0} = \begin{cases} (3.85714, 2.629369, 10.33333), & x < -0.8, \\ (1.0 + \epsilon \sin(\kappa \pi x), 0, 1.0), & x \geq -0.8, \end{cases} \qquad (3.21)$$

where $\epsilon = 0.2$ is the amplitude and $\kappa = 5$ the angular wave number. Although there is no exact solution to this problem, we took the accurate solution as the result given by the highly accurate FPM-RSK method [40], which was calibrated by the 5th order WENO scheme [23] for this problem.

Because of the complicated fluctuation post the shock, it is difficult for low order
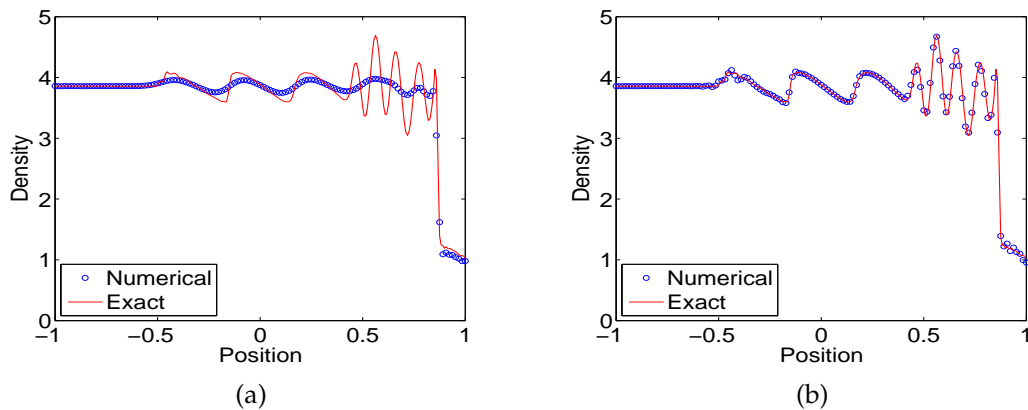
Figure 11: Solution to the Shu-Osher problem ($t = 0.47$, $\Delta t = 0.001$, 129 grid points). (a) Obtained with the 2nd-order PDE transform; (b) Obtained with the 10th-order PDE transform.

schemes to capture various frequencies of wave post shock as well as the sharp shock front [23]. High order methods, such as the 5th order WENO scheme [23] and the FPM-RSK method perform extremely well [40].

In the present work, we are interested in the understanding of the performance of the PDE transform of different orders. In fact, through our numerical tests, we found that when one uses the second order PDE transform, one cannot obtain a satisfactory numerical result, no matter what propagation time is chosen. With various choices of the propagation time, the second order PDE transform either damps the amplitude of high frequency waves too much or cannot prevent the solution from blowing up as time evolves. Fig. 11(a) shows the result of a 2nd-order PDE transform. The L_∞ error is 0.82. It is seen that it not only smooths the low frequency waves but also damps the high frequency components.

By contrast, high order PDE transforms work much better. As an illustration, Fig. 11(b) presents the result from a 10th order PDE transform. The L_∞ error is 0.11 occurred at the low frequency wave part. Obviously, the 10th-order PDE transform is able to well capture the complicated high-frequency waves post the shock. Furthermore, the shock front remains sharp in high-order PDE transforms. Although there is some abnormal oscillation at the on-set of low frequency waves, the 10th order PDE transform preserves the majority of the low frequency waves. This difficult case further validates the power of the present PDE transform.

3.3 2D Euler systems

In two spatial dimensions, we consider the Euler equation in the conservative form of

$$U_t + F(U)_x + G(U)_y = 0 \qquad (3.22)$$

with

$$U = \begin{pmatrix} \rho \\ \rho u \\ \rho v \\ E \end{pmatrix}, \quad F(U) = \begin{pmatrix} \rho \\ \rho u \\ \rho v \\ E \end{pmatrix} u + \begin{pmatrix} 0 \\ p \\ 0 \\ pu \end{pmatrix}, \quad G(U) = \begin{pmatrix} \rho \\ \rho u \\ \rho v \\ E \end{pmatrix} v + \begin{pmatrix} 0 \\ 0 \\ p \\ pv \end{pmatrix}, \quad (3.23)$$

where (u,v) is the fluid velocity and p is given by

$$p = (\gamma - 1)\left[E - \frac{1}{2}\rho(u^2 + v^2)\right]. \tag{3.24}$$

We discretize the conservative quantities $(\rho, \rho u, \rho v, p)$ on the mesh and applied the PDE transform during the time integration.

Like the one dimensional problems, the non-periodic domain in 2D can also be handled by symmetrical extension to the auxiliary domain. In more details, suppose the original domain is discretized by $N_1 \cdot N_2$ grid points indicated by (i,j) with $i = 1, \cdots, N_1 + 1$ and $j = 1, \cdots, N_2 + 1$. If the 2D domain is non-periodic in only one of the two directions, suppose in x-direction, then the computation domain is doubled with $2N_1 \cdot (N_2 + 1)$ grid points and $F(U), G(U)$ and u are extended by

$$\{F(U)\}_{i,j,k} = \{F(U)\}_{2N_1+2-i,j,k}, \qquad i = N_1+2, \cdots, 2N_1, \tag{3.25}$$

$$\{G(U)\}_{i,j,k} = \{G(U)\}_{2N_1+2-i,j,k}, \qquad i = N_1+2, \cdots, 2N_1, \tag{3.26}$$

$$\{U\}_{i,j,k} = \{U\}_{2N_1+2-i,j,k}, \qquad i = N_1+2, \cdots, 2N_1. \tag{3.27}$$

If the 2D domain is non-periodic in both two directions, then the computation domain is doubled with $2N_1 \cdot 2N_2$ grid points and $F(U)$, $G(U)$ and U are extended by

$$\{F(U)\}_{i,j,k} = \begin{cases} \{F(U)\}_{2N_1+2-i,j,k}, & i = N_1+2, \cdots, 2N_1, \\ \{F(U)\}_{i,2N_2+2-j,k}, & j = N_2+2, \cdots, 2N_2, \end{cases} \tag{3.28}$$

$$\{G(U)\}_{i,j,k} = \begin{cases} \{G(U)\}_{2N_1+2-i,j,k}, & i = N_1+2, \cdots, 2N_1, \\ \{G(U)\}_{i,2N_2+2-j,k}, & j = N_2+2, \cdots, 2N_2, \end{cases} \tag{3.29}$$

$$\{U\}_{i,j,k} = \begin{cases} \{U\}_{2N_1+2-i,j,k}, & i = N_1+2, \cdots, 2N_1, \\ \{U\}_{i,2N_2+2-j,k}, & j = N_2+2, \cdots, 2N_2. \end{cases} \tag{3.30}$$

3.3.1 Example 8 (2D Shock-entropy interaction)

Having tested the performance of the PDE transform for 1D shock-entropy interactions, we now consider the case in a 2D setting. The weak entropy wave makes an angle $\theta \in (0, \pi/2)$ against the x-axis. If $\theta = 0$, then this 2D problem essentially degenerates into the 1D shock-entropy problem studied earlier. Since now the entropy waves are oblique to the shock, this 2D problem is more challenging to resolve. Our objective is to further examine the capability of the PDE transform for higher dimensional problems.
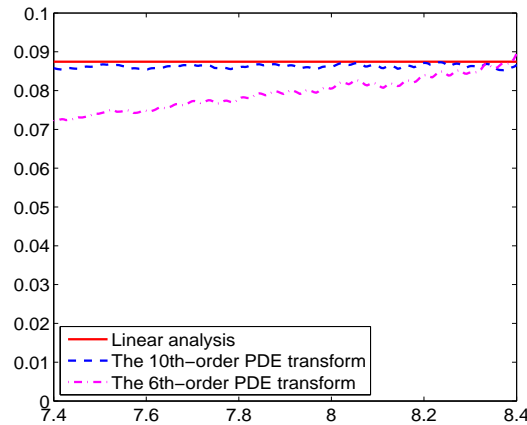
Figure 12: The amplitude of entropy waves in the 2D shock-entropy interaction problem obtained from PDE transforms of different orders.

Given the right state of the shock as $(\rho_r, u_r, v_r, p_r) = (1, 0, 0, 1)$, a weak entropy is added by changing the density on the right. Here ρ_r is modified by

$$\rho = \rho_r e^{-\epsilon \sin(\kappa z(\theta))/p_r}, \tag{3.31}$$

where $z(\theta)$ is related to the angle θ by $z(\theta) = x\cos\theta + y\sin\theta$ and ϵ and κ are the amplitude and wave number of the entropy wave, respectively. In this test, we choose parameters $\theta = \pi/6$, $\epsilon = 0.1$ and $\kappa = 15$.

For the computation domain, on the one hand, in order to implement the periodic boundary condition along the y-direction, the computation domain in y is set to be $[0, \frac{2\pi}{\kappa \sin\theta}]$ provided $\theta \neq 0$. On the other hand, the computation domain in x is set as $[0, 9]$.

Since the boundary condition in x is non-periodic, we extend the computation domain in x symmetrically from $[0, 9]$ to $[0, 18]$. We deploy 32 points in $[0, \frac{2\pi}{\kappa \sin\theta}]$ and 1024 points over $[0, 18]$, which implies 513 points over $[0, 9]$. In our test, the shock starts at $x = 0.5$ and moves up to $x = 8.5$. As we mentioned in the 1D case, a good numerical scheme should be able to preserve the amplitude of the high-frequency entropy waves. It needs to be mentioned that low-order methods do not work well for this problem [23]. Low-order methods would severely damp the amplitude as pointed out in Ref. [23].

For the PDE transform approach, methods of different PDE orders exhibit sharply different behaviors. Fig. 12 shows the performance of the 6th-order PDE transform by checking the maximum amplitude of the amplified waves along the y-direction for grid points $x \in [7.4, 8.4]$, and furthermore comparing with the amplitude predicted by the linear analysis, i.e., 0.08744786. It is seen that the 6th-order method has an obvious amplitude loss. In fact, to preserve the amplitude of the entropy waves, a high order PDE transform is preferred. We improve the performance by resorting to the 10th-order PDE transform. The result from the 10th-order PDE transform is also illustrated in Fig. 12. From this result, it is obvious that the amplitude of entropy waves is well maintained in the

post-shock region. Although there are small peaks and valleys, such a trivial deficiency appears in other methods as well [23, 40] and is acceptable. This test further validates the capability of the present PDE transform for resolving the shock entropy problem in a higher dimension.

3.3.2   Example 9 (2D Shock-vortex interaction)

Finally, we consider the problem of the interaction between a stationary shock and vortex. This problem has attracted much attention from numerous researchers because of its potential applications. This is another problem that poses challenges to low order numerical schemes. High order methods, such as WENO methods [23], spectral methods [40] and CFOR-Hermite scheme [62] work well for this problem. Here we further examine the capability of proposed PDE transforms for shock-vortex interactions.

The set up of the problem is as follows. The original computational domain is set to $[0,1] \times [0,1]$ with a stationary normal shock at $x = 0.5$ normal to x-axis. A flow with Mach number $M_s = 1.1$ enters at the inlet from the left and the shock is initialized as $(\rho_l, u_l, v_l, p_l) = (1, 1.1\sqrt{\gamma}, 0, 1)$ on the left state. A vortex centered at $(x_c, y_c) = (0.25, 0.5)$ is generated by introducing a perturbation to the original velocity field (u, v), temperature T and entropy S. We denote the perturbation by (u', v', T', S'), which is given as

$$(u', v') = \epsilon \tau e^{\alpha(1-\tau^2)} (\sin\theta, -\cos\theta),$$

$$T' = -\frac{(\gamma-1)}{4\gamma\alpha} \epsilon^2 e^{2\alpha(1-\tau^2)},$$

$$S' = 0, \tag{3.32}$$

where, $\tau = r/r_c$, $r = \sqrt{(x-x_c)^2 + (y-y_c)^2}$ and $\theta = \tan^{-1}[(y-y_c)/(x-x_c)]$. By the relation of $T = p/\rho$ and $S = \ln p/\rho^{\gamma}$, the perturbation ρ' and p' to initial ρ and p can be derived from T' and S'. Here ϵ and α are the strength and decay rate of the vortex and r_c is a parameter to regulate the strength of the vortex. In our test, we take $\epsilon = 0.3$, $\alpha = 0.204$ and $r_c = 0.05$.

The computational domain $[0,1] \times [0,1]$ is extended to $[0,2] \times [0,2]$ and discretized with an even-spacing Cartesian mesh. We use 129 even-spacing grid points in y domain of $[0,1]$ and 257 grid points in x domain of $[0,1]$. The mesh in the x direction is shifted by the Robert transformation [1] to deploy more mesh points towards the stationary shock. The upper and lower boundaries are imposed with the reflective boundary conditions. The time step in our integration is regulated by the CFL condition (CFL=0.5).

This problem prefers moderately high order PDE transforms because of its complicated feature. In fact, we cannot find satisfactory results from low-order PDE transforms yet. As an illustration, Fig. 13 depicts our results obtained with a 10th-order PDE transform. We plot the pressure profile with 20 contours at $t = 0.05, 0.2, 0.35, 0.6$.

From Fig. 13, it is seen that the solution is essentially free of oscillations. It can also be observed that the deformation of the vortex at the shock and the bifurcation after the shock are quite well captured.

(a) $t = 0.05$ (b) $t = 0.2$

(c) $t = 0.35$ (d) $t = 0.6$
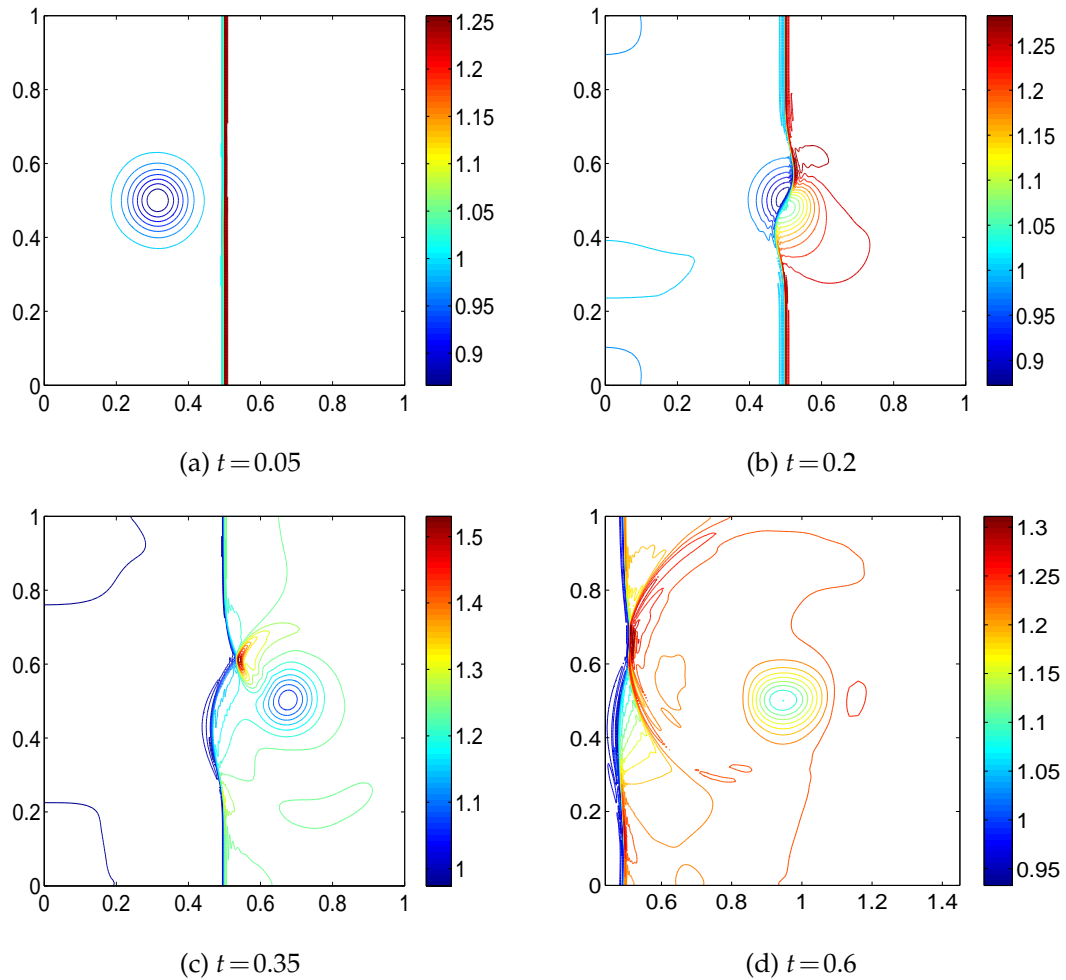
Figure 13: The pressure profile of 2D shock-vortex interaction problem from the 10th-order PDE transform (20 contours).

4 Concluding remarks

Systems of hyperbolic conservation laws are of fundamental importance in science and engineering. The construction of accurate, efficient and reliable numerical schemes has been an active research topic in applied mathematics over the past half a century. Due to a vast variety of complex problems with extremely diversified physical origins, many hyperbolic conservation law systems remain a challenge to mathematical methods. Typical examples include shock-turbulence interactions which involve a wide range of spatial scales and possible blow ups due to the successive amplification of exponentially small numerical errors during the time integration.

The present work introduces the use of evolution partial differential equations (PDEs) as a means to efficiently suppress Gibbs' oscillations in the numerical solution of hyperbolic conservation laws. Specifically, during the time integration of a hyperbolic conservation law system, an intermediate numerical solution at a given time step may be used as an initial data for a special evolution PDE. Then the solution of such an evolution PDE is accepted as an updated numerical solution at the given time step. Our approach involves the use of the PDE transform, a technique developed in our recent work [47, 49] for the mode decomposition of signals, image, and data. The PDE transform is based on a family of arbitrarily high order nonlinear PDEs originally introduced by Wei in 1999 [51] and a recursive scheme for reinitializing the input data [47, 48]. Like the wavelet transform, the PDE transform is able to decompose signals, images and data into functional modes, such as edges, trend, texture and feature with controllable frequency ranges and time-frequency localizations, which correspond to appropriate multiresolution analysis in the physical domain. Similarly, the PDE transform also has a prefect reconstruction of original signals, images and data. The PDE transform has found its success in signal processing [47, 49], image analysis [47, 49] and biomolecular surface construction [60].

It may appear computationally inefficient to suppress Gibbs' oscillations at a time step of integrating a hyperbolic conservation law equation by solving another evolution PDE. However, this is not true. Two techniques are proposed to improve the efficiency of the present approach. First, we use an adaptive measure of total variations to automatically determine whether the PDE transform is needed at each time step. Additionally, we utilize a fast PDE transform, which offers the analytical solution of an arbitrarily high order evolution PDE in the Fourier representation. This technique bypasses the stability constraint of solving high order evolution PDEs. Consequently, the present PDE transform algorithm is at least as efficient as our previous windowed Fourier pseudospectral method (FPM) [40] and is slightly more efficient than our earlier conjugate filter oscillation reduction (CFOR) scheme [18, 54, 61, 62].

To be more specific about the efficiency, since the FPM with the fast Fourier transform (FFT) is utilized as the spatial discretization, the complexity of the present PDE transform coupled with the FFT is of $O(N \ln N)$. This feature endows the proposed method with high efficiency, which is desirable for large scale problems in scientific and engineering applications.

A variety of benchmark tests are employed in the present work to validate the proposed approach, ranging from scalar conservation law systems to Euler equations in one and two spatial dimensions. Among these problems, Examples 2-5 typically prefer low-order shock capturing schemes; whereas Examples 1, and 6-9 are well known to require high order numerical methods. For example, low order schemes will severely damp the amplitude of the entropy waves in the shock-entropy interaction described by the Euler equation. The proposed PDE transform based FPM works extremely well for these two types of problems. For instance, it provides some of the best results for solving the Burgers' equation with non-convex flux. Furthermore, only about 5 points per wavelength (PPW) is needed for the present approach to handle the interaction of

shock-entropy waves and shock-vortex interactions. To our knowledge, the only other shock-capturing schemes that have demonstrated their ability of operating at 5 PPW are the CFOR scheme [18, 54, 61, 62] and the windowed FPM [40] proposed in our previous work. The performance of the proposed method is compared with those of the CFOR scheme [62] and the windowed FPM [40].

In order to make the present PDE transform based FPM working well for all of the above mentioned problems, we adjust two controlling parameters: the highest order of the PDE transform and the propagation time. In fact, the former is the primary parameter and the latter is less important although indispensable. It is found that the FPM behaves as a low order shock capturing scheme when it is coupled with a relatively low order PDE transform; while it behaves as a high order shock capturing scheme when it is coupled with a moderately high order PDE transform. The preferred orders of the PDE transform for these test examples are in a similar range of orders used in our PDE transform based molecular surface construction [60]. Unlike the signal decomposition, which requires the use of extremely high order PDE transforms [47, 49], the present systems of hyperbolic conservation laws do not need extremely high order PDE transforms. In fact, it is found that the use of extremely high order PDE transforms leads to unphysical oscillations. The selection of PDE transform parameters for all test examples is summarized in the Appendix, where the propagation time is optimized for each given order of the PDE transform.

As an introduction of the present PDE transform approach for systems of hyperbolic conservation laws, we only consider one and two dimensional problems in the present work. The extension of the present method to higher dimensions is feasible. However, this aspect is beyond the scope of the present paper.

It is possible to implement the PDE transform in the physical domain. However, this algorithm can be subject to stringent stability constraints of integrating high order PDEs. For example, if we solve the 10th-order PDE transform in the physical domain, then the constraint on the time step Δt is as small as the magnitude $(\Delta x)^{10}$, which causes the realization of the 10th-order PDE transform too costly. As a result, implicit time discretization methods such as alternating-direction-implicit (ADI) technique may be required to speed up the solution of the PDE transform.

It is also possible to automatically select the order of PDE transform during the time integration. Such an approach is useful and efficient for nonlinear conservation law systems with time-varying spectral distributions, such as the shock-vortex interaction discussed in the last example. If implemented, this adaptive PDE transform method could significantly expand the applicability of the proposed method for simulating the shock/turbulence interaction or more general flows with growing multi-scale vortices or other fine local structures. However, it is a major job to make this adaptive PDE transform method robust for a wide range of problems. Therefore, we recommend it as a future work.

It should be noted that the concrete expression of PDE transform is flexible, which enables the PDE transform to open to various applications. Beside the linear form in the

present work, there are different nonlinear forms to study. One potential form is the equations of geometry flow, such as the Minkowski curvature flow, Gauss curvature flow and Ricci flow. It has been demonstrated in the work by Z. Chen etc [7,8], that the geometry flow equation refines the geometric feature with application to solute-solvent interface in the implicit solvation model. The advantage of geometry flow equation based nonlinear PDE transform is that it enables the geometric feature embedding for the physical domain. It is still an open questions how the geometry flow equation based nonlinear PDE transform affects the solution of hyperbolic conservation law. However, this interesting topic is beyond the reach of the present paper and open for future study.

Finally, we would like to point out that the idea of using PDE transforms for hyperbolic conservation laws not only can be implemented with the FPM, but also can be paired with essentially any other relatively high order discretization schemes.

Acknowledgments

Appendix

In this Appendix, we list all the PDE transform parameters, i.e., the highest order $l = 2m$ and the propagation time τ, used in the present work for 9 test examples.

In our implementation, the wavenumber w is set by $w_q = (2\pi q/N)/\Delta$, $q = -N/2, \cdots,$ $1, \cdots, N/2 - 1$ where L is the length of computation domain, N is the number of discretized grid points and $\Delta = L/N$ is the grid spacing. This series of wavenumbers ranges over $[-\pi/\Delta, \pi/\Delta)$. The design of PDE transform depends on the order n and propagation time τ. Table 3 lists the order l and propagation time τ used in each test problem. To better interpret the frequency response, we rescaled the wavenumber w from $[-\pi/\Delta, \pi/\Delta)$ to $[-\pi, \pi)$. Consequently, the propagation time τ is rescaled to $\tau^* = \tau/(\Delta)^l$ correspondingly.

References

[1] D. A. Anderson, J. C. Tannehill, and R. H. Pletcher. Computational Fluid Mechanics and Heat Transfer. McGraw-Hill, New York, 1984.

[2] P. W. Bates, G. W. Wei, and S. Zhao. Minimal molecular surfaces and their applications. J. Comput. Chem., 29(3):380–91, 2008.

[3] F. Bianco, G. Puppo, and G. Russo. High-order central differencing for hyperbolic conservation laws. SIAM J. Sci. Comput., pages 294–322, 1999.

[4] W. Cai and C. W. Shu. Uniform high-order spectral methods for one- and two-dimensional euler equations. J. Comput. Phys., 104:427–443, 1993.

Table 3: The order and propagation time of the PDE transform used in test examples.

Example No	Case	Order	Propagation time when $w \in [-\pi/\Delta, \pi/\Delta)$	Rescaled propagation time when $w \in [-\pi, \pi)$
1	$\kappa = 5, 10$	6	1.0E-13	6.8E-03
	$\kappa = 20, 25$	12	1.0E-20	4.7E-03
2		2	1.0E-05	1.6E-01
		4	1.0E-12	2.6E-04
		6	1.0E-16	4.4E-04
		8	1.0E-20	7.2E-04
3	$u_l = 1, u_r = 0$	6	3.0E-15	1.2E-03
	$u_l = 0, u_r = 1$	6	7.5E-10	5.3E-02
4		4	5.5E-14	1.0E-03
		6	6.0E-18	5.9E-05
5	Sod's	6	1.0E-09	4.4E-03
	Lax's	6	1.0E-10	4.4E-04
6	$\kappa = 18$	12	3.0E-27	3.4E-06
	$\kappa = 32$	12	1.5E-30	7.0E-06
		6	5.0E-16	1.0E-03
		40	1.0E-95	1.7E-13
	$\kappa = 60$	12	2.0E-34	3.8E-06
7		10	1.0E-23	1.1E-05
		2	5.0E-06	2.0E-02
8		10	3.5E-23	1.2E-05
		6	1.0E-14	3.3E-04
9		10	1.0E-24	1.1E-03

[5] C. Canuto, M. Y. Hussaini, A. Quarteroni, and T. A. Zang. Spectral methods in fluid dynamics. Springer-Verlag, Berlin, 1988.

[6] D. Chen, G. W. Wei, X. Cong, and G. Wang. Computational methods for optical molecular imaging. Commun. Numer. Meth. Engng., 25:1137–1161, 2009.

[7] Z. Chen, N. A. Baker, and G. W. Wei. Differential geometry based solvation models I: Eulerian formulation. J. Comput. Phys., 229:8231–8258, 2010.

[8] Z. Chen, N. A. Baker, and G. W. Wei. Differential geometry based solvation models II: Lagrangian formulation. J. Math. Biol., 63:1139–1200, 2011.

[9] S. Didas, J. Weickert, and B. Burgeth. Properties of higher order nonlinear diffusion filtering. J. Math. Imaging Vis., 35(3):208–226, 2009.

[10] W. S. Don. Numerical study of pseudospectral methods in shock wave applications. J. Comput. Phys, 110:103–111, 1994.

[11] W. S. Don and D. Gottlieb. Spectral simulation of supersonic reactive flows. SIAM J. Numer Anal., 35:2370–2384, 1998.

[12] B. Fornberg. A Practical Guide to Pseudospectral Methods. Cambridge University Press, Cambridge, 1996.

[13] D. Gottlieb and J. S. Hesthaven. Spectral methods for hyperbolic problems. J. Comput. Appl. Math., 128:83–131, 2001.

[14] D. Gottlieb, L. Lustman, and S. A. Orszag. Spectral calculations of one-dimensional inviscid compressible flow. SIAM J. Sci. Stat. Comput., 2:296–310, 1981.

[15] D. Gottlieb, C. W. Shu, A. Solomonoff, and H. Vandeven. On the Gibbs phenomenon I. J. Comput. Appl. Math., 43:81–98, 1992.

[16] D. Gottlieb and E. Tadmor. Recovering pointwise values of discontinuous data within spectral accuracy. Progress and Supercomputing in Computational Fluid Dynamics, E. M. Murman and S. S. Abarbanel eds., Birkhäuser, pages 357–375, 1985.

[17] T. Grahs and T. Sonar. Entropy-controlled artificial anisotropic diffusion for the numerical solution of conservation laws based on algorithms from image processing. J. Vis. Commun. Image R., 13:176–194, 2002.

[18] Y. Gu and G. W. Wei. Conjugated filter approach for shock capturing. Commun. Numer. Meth. Engng., 19:99–110, 2003.

[19] Y. Gu, Y. C. Zhou, and G. W. Wei. Conjugate filters with spectral-like resolution for 2D incompressible flows. Comput. Fluids, 33:777–794, 2003.

[20] A. Harten, B. Engquist, S. Osher, and S. Chakravarthy. Uniform high-order accurate essentially non-oscillatory schemes, III. J. Comput. Phys., 131:3–47, 1997.

[21] G. Hu, R. Li, and T. Tang. A robust weno type finite volume solver for steady euler equations on unstructured grids. Commun. Comput. Phys., 9:627–648, 2011.

[22] M. Y. Hussaini, D. A. Kopriva, M. D. Salas, and T. A. Zang. Spectral methods for the euler equation: Part I - Fourier methods and shock-capturing. AIAA J., 23(No. 1):64–70, 1985.

[23] G. S. Jiang and C. W. Shu. Efficient implementation of weighted ENO schemes. J. Comput. Phys., 126(1):202–228, 1996.

[24] S. Jin and C. D. Levermore. Numerical schemes for hyperbolic conservation laws with stiff relaxation terms. J. Comput. Phys., 126:449–467, 1996.

[25] S. T. Johansen, J. Y. Wu, and W. Shyy. Filter-based unsteady rans computations. Int. J. Heat Fluid Flow, 25:10–21, 2004.

[26] R. Krasny. A study of singularity formation in a vortex sheet by the point vortex approximation. J. Fluid Mech., 167:65–93, 1986.

[27] A. Kurganov and D. Levy. A third-order semidiscrete central scheme for conservation laws and convention diffusion equations. SIAM J. Sci. Comput., 22:1461–1488, 2000.

[28] S. Lee, S. K. Lele, and P. Moin. Interaction of isotropic turbulence with shock waves: Effect of shock strength. J. Fluid Mech., 340:225–247, 1997.

[29] R. J. LeVeque and M. Pelanti. A class of approximate riemann solvers and their relation to relaxation schemes. J. Comput. Phys., 172:574–591, 2001.

[30] J. Li, Q. Li, and K. Xu. Comparison of the generalized riemann solver and the gas-kinetic scheme for inviscid compressible flow simulations. J. Comput. Phys., 230:5080–5099, 2011.

[31] X. D. Liu and E. Tadmor. Third order non-oscillatory central scheme for hyperbolic conservation laws. Numer. Math., 79:397–425, 1998.

[32] M. Lysaker, A. Lundervold, and X. C. Tai. Noise removal using fourth-order partial differential equation with application to medical magnetic resonance images in space and time. IEEE T. Image Process., 12(12):1579–1590, 2003.

[33] J. F. McKenzie and K. O. Westphal. Interaction of linear waves with oblique shock waves. Phys. Fluids, 11:2350–2362, 1968.

[34] H. Nessyahu and E. Tadmor. Non-oscillation central differencing for hyperbolic conservation laws. J. Comput. Phys., 87:408–463, 1990.

[35] G. Ni, S. Jiang, and K. Xu. A dgbgk scheme based on weno limiters for viscous and inviscid flows. J. Comput. Phys., 227:5799–5815, 2008.

[36] P. Nithiarasu, O. C. Zienkiewicz, B. V. K. S. Sai, K. Morgan, R. Codina, and M. Vazquez. Shock capturing viscosities for the general fluid mechanics algorithm. Int. J. Numer. Meth. Fluids, 28:1325–1353, 1998.

[37] J. M. Qiu and C. W. Shu. Conservative high order semi-lagrangian finite difference WENO methods for advection in incompressible flow. J. Comput. Phys., 230:863–889, 2011.

[38] J. X. Qiu and C. W. Shu. On the construction, comparison, and local characteristic decomposition for high order central WENO schemes. J. Comput. Phys., 183:187–209, 2002.

[39] L. I. Rudin, S. Osher, and E. Fatemi. Nonlinear total variation based noise removal algorithms. Physica D, 60(1-4):259–268, 1992.

[40] Y. H. Sun, P. R. Wu, G. W. Wei, and G. Wang. Evolution-operator-based single-step method for image processing. Int. J. Biomed. Imaging, 83847:1–27, 2006.

[41] Y. H. Sun, Y. C. Zhou, S. G. Li, and G. W. Wei. A windowed fourier pseudospectral method for hyperbolic conservation laws. J. Comput. Phys., 214:466–490, 2006.

[42] E. Tadmor. Convergence of spectral methods for nonlinear conservation laws. SIAM J. Numer. Anal., 26:30–44, 1989.

[43] E. F. Toro, R. C. Millington, and V. A. Titarev. Ader: Arbitrary-order non-oscillatory advection scheme. Proc. 8th International Conference on Non-linear Hyperbolic Problems, Magdeburg, Germany, March, 2000.

[44] L. N. Trefethen. Spectral Methods in Matlab. Oxford University, Oxford, England, 2000.

[45] H. Vandeven. Family of spectral filters for discontinuous problems. J. Sci. Comput., 6:159–192, 1991.

[46] D. C. Wan, B. S. V. Patnaik, and G. W. Wei. Discrete singular convolution-finite subdomain method for the solution of incompressible viscous flows. J. Comput. Phys., 180:229–255, 2002.

[47] Y. Wang, G. W. Wei, and S.-Y. Yang. Partial differential equation transform – Variational formulation and Fourier analysis. Int. J. Numer. Meth. Biomed. Engng., 27:1996–2020, 2011.

[48] Y. Wang, G. W. Wei, and S.-Y. Yang. Iterative filtering decomposition based on local spectral evolution kernel. J. Sci. Comput., 50:629–664, 2012.

[49] Y. Wang, G. W. Wei, and S.-Y. Yang. Mode decomposition evolution equations. J. Sci. Comput., 50:495–518, 2012.

[50] G. W. Wei. Discrete singular convolution for the solution of the Fokker-Planck equations. J. Chem. Phys., 110:8930–8942, 1999.

[51] G. W. Wei. Generalized Perona-Malik equation for image restoration. IEEE Signal Proc. Letters, 6(7):165–167, 1999.

[52] G. W. Wei. Oscillation reduction by anisotropic diffusions. Comput. Phys. Commun., 144:317–342, 2002.

[53] G. W. Wei. Differential geometry based multiscale models. B. Math. Biol., 72:1562 – 1622, 2010.

[54] G. W. Wei and Y. Gu. Conjugated filter approach for solving Burgers' equation. J. Comput. Appl. Math., 149:439–456, 2002.

[55] G. W. Wei and Y. Q. Jia. Synchronization-based image edge detection. Europhysics Letters, 59(6):814–819, 2002.

[56] G. W. Wei, Y. B. Zhao, and Y. Xiang. Discrete singular convolution and its application to the analysis of plates with internal supports, I theory and algorithm. Int. J. Numer. Meth. Engng., 55:913–946, 2002.

[57] G. W. Wei, Q. Zheng, Z. Chen, and K. Xia. Variational multiscale models for charge transport. SIAM Review, 54:699–754, 2012.

[58] K. Xu. A gas-kinetic BGK scheme for the Navier-Stokes equations and its connection with artificial dissipation and Godunov method. J. Comput. Phys., 171:289–335, 2001.

[59] H. C. Yee, N. D. Sandham, and M. J. Djomehri. Low-dissipative high-order shock-capturing methods using characteristic-based filters. J. Comput. Phys., 150:199–238, 1999.

[60] Q. Zheng, S. Y. Yang, and G. W. Wei. Molecular surface generation using PDE transform. Int. J. Numer. Meth. Biomed. Engng., 28:291–316, 2012.

[61] Y. C. Zhou, Y. Gu, and G. W. Wei. Shock-capturing with natural high frequency oscillations. Int. J. Numer. Meth. Fluid, 41:1319–1338, 2003.

[62] Y. C. Zhou and G. W. Wei. High resolution conjugate filters for the simulation of flows. J. Comput. Phys., 189:159–179, 2003.